Generation of global 1 km all-weather instantaneous and daily mean land surface temperature from MODIS data

Bing Li[1], Shunlin Liang[2], Han Ma[2], Guanpeng Dong[1], Xiaobang Liu[3], Tao He[4], Yufang Zhang[5]

[1] Key Research Institute of Yellow River Civilization and Sustainable Development & Collaborative Innovation Center on Yellow River Civilization of Henan Province, Henan University, Kaifeng, 475001, China

[2] Department of Geography, University of Hong Kong, Hong Kong 999077, China

[3] The 27th Research Institute of China Electronics Technology Group Corporation, Zhengzhou 450047, China

[4] School of Remote Sensing and Information Engineering, Wuhan University, Wuhan 430079, China

[5] School of Software, Northwestern Polytechnical University, Xi'an 710072, China

Correspondence to: Shunlin Liang (shunlin@hku.hk)

Abstract: Land surface temperature (LST) serves as a crucial variable in characterizing climatological, agricultural, ecological, and hydrological processes. Thermal infrared (TIR) remote sensing provides high temporal and spatial resolution for obtaining LST information. Nevertheless, TIR-based satellite-LST products frequently exhibit missing values due to cloud interference. Prior research on estimating all-weather instantaneous LST has predominantly concentrated on regional or continental scales. This study involved generating a global all-weather instantaneous and daily mean LST product spanning from 2000 to 2020 using XGBoost. Multisource data, including Moderate-Resolution Imaging Spectroradiometer (MODIS) top-of-atmosphere (TOA) observations, surface radiation products, and reanalysis data, were employed. Validation using an independent

25 dataset of 77 individual stations demonstrated the high accuracy of our products, yielding RMSEs

26 of 2.787 K (instantaneous) and 2.175 K (daily). The RMSE for clear-sky conditions was 2.614 K

27 for the instantaneous product, slightly lower than the cloudy-sky RMSE of 2.931 K. Our

28 instantaneous and daily mean LST products exhibit higher accuracy compared to the MODIS

29 official LST product (RMSE=3.583 K instantaneous, 3.105 K daily) and the land component of the

30 5th generation of European ReAnalysis (ERA5-Land) LST product (RMSE= 4.048 K instantaneous,

31 2.988 K daily). Significant improvements are observed in our LST product, notably at high latitudes,

32 compared to the official MODIS LST product. The LST dataset from 2000 to 2020 at the monthly

33 scale, the daily mean LST on the first day of 2010 can be freely downloaded from

34 https://doi.org/10.5281/zenodo.4292068(Li et al. 2024), and the complete product will be available

35 at https://glass-product.bnu.edu.cn/.

37 **Keywords: land surface temperature, all-weather, global, XGBoost, MODIS**

1 Introduction:

Land surface temperature (LST) is the skin temperature of the Earth's surface, and one of the crucial parameters in the surface energy balance, and the hydrothermal cycle (Bastiaanssen et al. 1998; Tomlinson et al. 2011). LSTs retrieval from in situ measurements or satellites are widely used in many scientific fields (Kappas and Phan 2018), such as climate change (Auger et al. 2021; Weng 2009), urban heat island (Zhou et al. 2018), drought monitoring (Wan et al. 2010), longwave radiation estimation (Cheng and Liang 2016), evapotranspiration (Kalma et al. 2008; Yao et al. 2012), soil moisture estimation (Zhang et al. 2015), and air temperature estimation (Chen et al. 2021; Rao et al. 2019; Shen et al. 2020). High-precision measurements of LST aid in the recording of the long-term global temperature trends, thus, the International Geosphere and Biosphere Programme (IGBP) lists it as one of its priority parameters (Townshend et al. 2007). Owing to the complex and rapid variation in temporal and spatial scales, in situ measurements cannot provide regional LST or capture the spatial variation in LST. Remote sensing has become the only way to obtain LST with high spatial and temporal resolution from regional to global scales (Li et al. 2013).

Over the past few decades, substantial advancements have been made in the inversion of LST from remote sensing satellites. The retrieval of satellite LST products is predominantly accomplished using thermal infrared (TIR) remote sensing data (Li et al. 2013). These LST products typically exhibit a notable spatial resolution, exemplified by the Visible Infrared Imaging Radiometer Suite (VIIRS) boasting a resolution of 750 meters, the Advanced Very High Resolution Radiometer (AVHRR) with 0.05° (Li et al. 2023a; Ma et al. 2020a), and the Moderate-Resolution Imaging Spectroradiometer (MODIS) satellite with a resolution of 1 kilometer (Wan 2014; Wan and Li 1997). Nevertheless, due to the constrained penetration capability of thermal radiation, TIR data is exclusively applicable for observing LST under clear-sky conditions. Global average annual cloud coverage has been reported to exceed 70% (Mercury et al. 2012). The lack of data has significantly constrained the application of LST products. Consequently, all-weather LST estimation is one of the difficulties that need to be solved urgently.

Besides data gaps due to cloud contamination, extending the temporal scale of LST poses a significant challenge in retrieving LST remote sensing products, requiring urgent attention. LST, a dynamic physical attribute, exhibits temporal variation. However, satellite-derived LST captures only instantaneous observations at specific times and angles. Instead of focusing solely on instantaneous LST,

68 certain researchers emphasize the importance of daily, monthly, or yearly average LST to track the impact

69 of increasing LST on glaciers, ice sheets, and vegetation within the Earth's ecosystem (Lawrimore et al.

70 2011). Currently, for MODIS LST products, there exist daily instantaneous L2 products, daily gridded

71 instantaneous L3 products, and eight-day synthetic products (Wan 2014). Nevertheless, there's an

72 absence of L4 products encompassing daily mean, monthly, and annual LST data. Hence, it holds

73 significant importance to estimate daily mean LST based on limited MODIS observations. Acquiring the

74 daily mean LST allows estimation of monthly or annual mean LST, crucial for prolonged monitoring

75 across diverse research domains like climate change, agriculture, and drought studies.

76   As for filling LST gaps under cloudy-sky conditions, researchers have explored various methods

77 (Li et al. 2023c). One type of approach is based on space-time information, such as interpolation and

78 fusion methods (Pede and Mountrakis 2018). Interpolation methods usually utilize temporally or

79 spatially proximate clear-sky pixel information to fill in the pixels under the cloudy-sky condition.

80 Nevertheless, the efficacy of the interpolation method is contingent upon the accessibility of clear-sky

81 pixels. The reconstruction outcomes prove less satisfactory in instances of extensive missing regions or

82 prolonged periods of cloud cover (Metz et al. 2014; Zhang et al. 2018; Zhang et al. 2022). In recent years,

83 spatiotemporal fusion methods have been explored for obtaining all-weather LST(Chen et al. 2015; Long

84 et al. 2020; Wu et al. 2019). The essence of spatiotemporal fusion for LST involves deriving high spatial

85 resolution LST at time t0 from its counterpart with coarse spatial resolution at the identical time instance,

86 achieved through the application of a scale conversion factor (Long et al. 2020; Wu et al. 2019). Due to

87 the algorithm's complexity, fusion methods are commonly evaluated within limited geographical scopes,

88 with their applicability constrained when extended to larger areas. Furthermore, both interpolation and

89 spatiotemporal fusion methods hinge on information derived from clear-sky pixels, yielding

90 reconstructed theoretical clear-sky LST rather than the real cloudy-sky LST. In order to obtain actual

91 LST under cloudy-sky conditions, one type of approach considering the physical processes of the surface

92 energy balance (SEB). Jin and Dickinson (2000) introduced a method utilizing SEB to account for

93 changes in solar radiation on LST during cloudy conditions. This approach corrects clear-sky LST using

94 the SEB equation to derive actual cloudy-sky LST. Over time, the SEB-based method has been refined

95 for geostationary satellites (Jia et al. 2022; Liu et al. 2023; Zhang et al. 2024) and MODIS data (Jia et al.

96 2021; Yu et al. 2014; Zeng et al. 2018). However, widespread application is limited due to gaps in data

97   coverage and the necessity of meteorological SEB parameters (e.g., air temperature, wind speed), which

98   are challenging to obtain accurate data on a large scale.

99   Apart from the mentioned methods for LST retrieval under cloudy-sky conditions, alternative

100   approaches utilize all-weather data like microwave data, reanalysis data, or model simulations to derive

101   the cloudy-sky information. Passive microwave (PMW) data are less affected by cloud contamination,

102   providing a possibility for all-weather LST estimations (De Jeu 2003; Duan et al. 2017b; Holmes et al.

103   2009). However, the existing microwave observations usually have coarse resolutions (e.g., AMSR-E

104   with 25km) (Mao et al. 2007). Since the land surface microwave emissivity is sensitive to land surface

105   characteristics and difficult to measure, the accuracy of the PMW LST data is relatively lower than that

106   of TIR LST(McFarland et al. 1990).In addition, PMW data basically have swath gaps, especially at low

107   latitudes, which makes it difficult to obtain full-coverage LST (Holmes et al. 2009; Zhou et al. 2015).

108   Thus, LST retrieval from PMW data cannot satisfy the requirements of high-precision and refined

109   applications. Some scholars have explored the possibility of combining PMW and TIR data to estimate

110   all-weather LST. These methods perform well at regional or national scales (Duan et al. 2017b; Wu et al.

111   2022; Xu and Cheng 2021; Zhang et al. 2020). However, owing to the availability of PMW data and the

112   complexity of algorithms, it is difficult to achieve long-term production at a global scale.

113   In comparison, reanalysis data can provide another way for all-weather LST estimation, with all-

114   weather observations, long-term and seamless characteristics. With the updating of reanalysis and

115   modeled data, spatial resolution and accuracy are improved (Muñoz-Sabater et al. 2021). Several studies

116   have attempted to utilize reanalysis data combined with TIR (Long et al. 2020; Tang et al. 2024; Zhang

117   et al. 2021) and PMW data (Zhang et al. 2020; Zhou et al. 2022) to obtain all-weather LST, which were

118   well implemented on the regional scale. In recent years, researchers have a growing interest in the

119   estimation of global all-weather LST. Shiff et al. (2021) integrated modeled temperature data to

120   supplement missing values in MODIS LST using the Google Earth Engine (GEE). Nevertheless, the

121   proposed approach solely addressed missing pixels, potentially introducing border effects. Globally,

122   continuous spatiotemporal LST data at a resolution of 0.05° have been generated, rectifying reconstructed

123   missing data under cloudy-sky conditions using reanalysis data (Yu et al. 2022). Additionally, global

124   seamless 8-day and monthly average LST data, featuring a 30 arcsecond resolution, were created by

125   integrating reanalysis data (Yao et al. 2023). These studies confirm the potential of reanalysis data for

126   estimating all-weather LST, yet there remains ample room for exploration at a spatiotemporal scale of

127   one kilometer per day.

128   Regarding daily mean LST, researchers have investigated acquiring it from polar-orbiting satellites.

129   Specifically, they have employed MODIS instantaneous LSTs to estimate the daily mean

130   LST(Williamson et al. 2014; Xing et al. 2021). The maximum-minimum method determined the daily

131   mean LST by averaging its maximum and minimum values, exhibiting a strong correlation with surface

132   air temperature (Williamson et al. 2014). Despite its relatively low accuracy, it presents a straightforward

133   means of estimating daily mean LST using the limited observations from polar orbiting satellites.

134   Another approach involves the diurnal temperature cycle (DTC), employing various nonlinear models

135   based on heat conduction and energy balance equations(Aires et al. 2004; Duan et al. 2012; Inamdar et

136   al. 2008; Sun and Pinker 2005), capable of retrieving daily mean LST. However, the DTC method

137   requires specific satellite observation counts within a daily cycle, existing challenges for all-weather

138   daily mean LST retrieval, especially for polar-orbiting satellites. Hong et al. (2021) proposed a

139   framework combining the annual temperature cycle (ATC) and DTC to retrieve all-weather daily mean

140   LST at a spatial resolution of 0.5°×0.5° (Hong et al. 2022). Xing et al. (2021) utilized global in situ

141   measurements and multiple linear regression to enhance the MODIS daily mean LST model accuracy

142   under clear-sky conditions. Then, Li et al. (2023b) integrated pre-2000 polar-orbiting satellite data to

143   improve the global daily mean LST model. Most mentioned methods are applicable exclusively under

144   clear-sky conditions, and all-weather estimation remains a challenge. Besides, the sine or cosine assumed

145   in the DTC and the multiple linear regression equations may not necessarily fit the relationship between

146   instantaneous observations and daily mean value. Thus, more appropriate relational models need to be

147   constructed. The main limitation of MODIS daily mean LST estimation has been their restricted

148   observations. MODIS data in swath type can provide more observations, which potentially improving

149   the accuracy, but few research has attempted it. Obtaining all-weather daily mean LST from polar-

150   orbiting satellite observations (e.g., MODIS), particularly at a global scale with a 1 km spatial resolution,

151   still remains a significant challenge.

152   Recently, machine learning and deep learning techniques have gained significant traction in remote

153   sensing due to their superior model fitting capabilities (Ma et al. 2019; Yuan et al. 2020). Scholars have

154   investigated LST retrieval using learning techniques across various satellite platforms (Li et al. 2021; Ma

155 et al. 2024; Mao et al. 2018; Wang et al. 2010). However, the majority of these methods utilized clear-

156 sky pixels as the true value to construct the model, possibly failing to capture the relationship under

157 cloudy-sky conditions. Additionally, learning methods have not yet been applied for estimating daily

158 mean LST. Our former research has estimated all-weather LST from MODIS data using a random forest

159 over the conterminous United States (Li et al. 2021). Considering the urgency of obtaining all-weather

160 LST on a large regional scale and expanding the daily mean time scale, this study refined our previously

161 developed algorithm for an all-weather instantaneous LST product and developed a new method for a

162 daily mean LST product at a global scale. The improvements over our previous study include: 1) More

163 sufficient information: MODIS top-of-atmosphere (TOA) information was taken into account; 2) Expand

164 the estimated LST time scale: a novel algorithm was proposed to estimate both instantaneous and daily

165 mean LST; and 3) Higher efficiency algorithm and larger region: the global all-weather LST products

166 were generated.

167   The rest of the paper is organized as follows. Section 2 describes the data used in this paper. Section

168 3 provides a summary of the proposed method. The results are presented in Section 4. A discussion part

169 is presented in Section 5. Section 6 is the data availability. Finally, Section 7 presents the conclusions.

170

 2 Data

172   In this study, the remote sensing data, reanalysis data and in situ measurements from 2002-

173   2018 were used to construct all-weather LST models. These data, spanning 2000 to 2020, along

174   with the developed models, were used to generate the instantaneous and daily mean LST products.

175   In situ measurements validated the accuracy of the proposed algorithm and the generated products.

176   The data used are described in detail as follows:

177   **2.1 Remotely sensed and reanalysis data**

178   The remote sensing data and reanalysis data used in this study are summarized in Table 1. Among

179   them, remote sensing data are mainly from official MODIS products and the Global LAnd Surface

180   Satellite (GLASS) product suite. MOD021KM and MYD021KM are MODIS TOA observational

181   datasets. The shortwave bands (B1–B7, B19) and longwave bands (B27–B36) were selected as model

182   inputs. Geolocation information was obtained from MODIS geolocation data (MOD03 and MYD03).

183   The coordinates from MODIS geolocation data were used to match up with products and in situ

184   measurements, while height, solar zenith angle, solar azimuth angle, view zenith angle and view azimuth

185   angle were used as the model inputs. MODIS LST (MOD11L2/MYD11L2) was used for the comparison

186   and identification of cloudy-sky conditions. The GLASS product suite includes at least 12 land surface

187   variables, which have high spatial resolutions (1 km and 0.05°), long-term temporal coverage (1981–

188   present), spatial continuity, and high quality (Liang et al. 2021; Liang et al. 2013a; Liang et al. 2013b).

189   In this study, we used the following four products from the GLASS product suite: Broad band emissivity

190   (BBE), broadband albedo (albedo), downward solar radiation (DSR), and downward thermal radiation

191   (LWDN). BBE product was used to obtain in-situ LST (Cheng and Liang 2013, 2014). Albedo was used

192   as the model input to describe surface characteristics (Liu et al. 2013a; Qu et al. 2016; Qu et al. 2014).

193   Because LST is affected by both solar radiation and surface longwave radiation, DSR and LWDN were

194   also used in the model construction (Cheng et al. 2017; Zhang et al. 2019).

195   In recent years, an enhanced global dataset for the land component of the fifth generation of

196   European ReAnalysis (ERA5-Land) has been developed (Hersbach et al. 2020; Muñoz-Sabater et al.

197   2021). ERA5-Land describes a consistent long terms evolution of water and energy cycles over land. It

198   was generated through global high-resolution numerical integrations of the European Centre for

199   Medium-Range Weather Forecasts (ECMWF) land surface model driven by the downscaled

meteorological forcing from the ERA5 climate reanalysis. Compared with the previous ERA-Interim (80

km) and ERA (31 km), ERA5-Land has a higher spatial resolution (9 km) and temporal resolution (1 h).

Because ERA5-Land LST includes worldwide and all-weather data, it was used in the model construction

as the background value and was also used for comparison. ERA5-Land LST is hereafter referred to as

ERA LST.

Table 1. Summary of remote sensing and reanalysis data

Product	Variables	Resolution (temporal /spatial)	Temporal coverage	Usage	Data link
MOD021KM /MYD021KM	Toa reflectance, brightness temperature	Instantaneous /1 km	2000-present for MODIS Terra / 2002-present for MODIS Aqua	Model inputs	https://earthdata.nasa.gov/
MOD03/ MYD03	Latitude, longitude, height,	Instantaneous /1 km		Model inputs/match up	
MOD11L2/ MYD11L2	LST	Instantaneous /1 km		Comparison	
GLASS	BBE	8 days/1km	2000-2022	Calculate in situ LSTs	http://glass.umd.edu/
GLASS	Albedo	8 days/1km	2000-2022	Model inputs	or
GLASS	DSR	Daily/0.05°	2000-2022	Model inputs	https://glass-product.bnu.edu.cn/
GLASS	LWDN	Instantaneous /1 km	2000-2020	Model inputs	
ERA5-land	LST	1 hour/ 9 km	1981-present	Model inputs	https://cds.climate.copernicus.eu/

2.2 In situ measurements

To obtain in situ LSTs, we collected upwelling and downwelling longwave radiation measurements

from 315 sites with different land cover types and geolocations on a global scale. Both instantaneous and

daily mean in situ LSTs were retrieved from in situ measurements. As shown in Fig.1, ground

measurements from 238 stations were used to develop the proposed network (blue circles), whereas the

measurements from the remaining 77 stations (red circles) were selected as independent validation

datasets to evaluate the performance of the trained model. The collection sites were mainly from eight

observation networks, which are described in the following paragraphs.
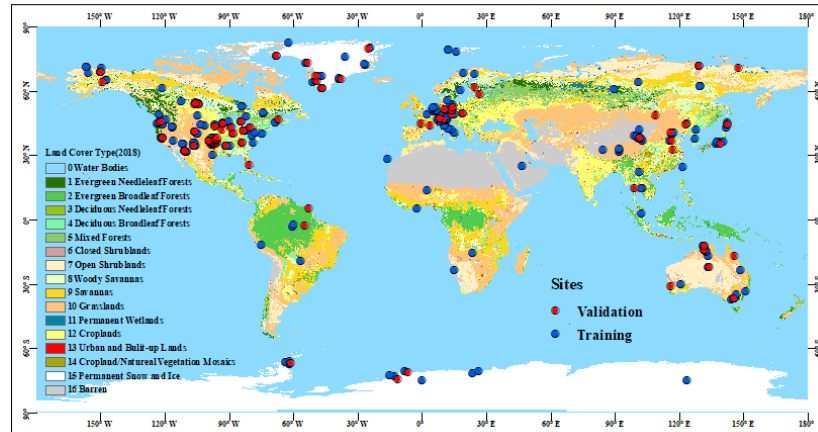
215

216   Fig.1 Spatial distribution of the selected sites at a global scale. Land use cover types of 2018 (background color shading) were
217   from the MODIS land use cover product MCD12C1. The site used for model training are shown with blue circles while the
218   separated validation sites are shown with red circles.

219   AmeriFlux (https://ameriflux.lbl.gov/) is a network of stations that continuously measures

220   ecosystem carbon dioxide, water, energy fluxes, and related environmental variables using eddy

221   covariance techniques (Baldocchi 2003). The network was launched in 1996, and was established to

222   connect research on field sites representing major climate and ecological biomes(Boden et al. 2013). The

223   network has more than past and present flux towers, and sites with longwave radiation measurements

224   were selected. These sites are distributed across North, Central, and South America. The observation

225   interval of these sites was half an hour.

226   FLUXNET (https://fluxnet.org/) is a global network of micrometeorological tower sites that uses

227   eddy covariance methods to measure carbon dioxide, water vapor, and energy fluxes (Baldocchi et al.

228   2001). It has more than 500 flux towers worldwide are operating on a long-term basis. The overarching

229   goal of the FLUXNET data collection is to provide information for validating remote sensing products,

230   such as net primary productivity and energy fluxes. Sites with longwave radiation records were used in

231   this study. The observation interval of the sites was half an hour.

232   The Baseline Surface Radiation Network (BSRN, https://bsrn.awi.de/) is a project of the Data and

233   Assessments Panel of the Global Energy and Water Cycle Experiment (GEWEX) under the umbrella of

234   the World Climate Research Programme (WCRP) (Ohmura et al. 1998). The purpose of this network is

235   to provide validation materials for satellite radiometry and climate models. It further aims to detect long-

236   term variations in the radiation field at the Earth's surface, which play a vital role in climate changes

237   (Driemel et al. 2018). The stations (currently 74 in total, 58 active) are distributed in contrasting climatic

zones, covering a latitude range from 80° N to 90° S. The required longwave radiation measurements were obtained with high accuracy and high time resolution (1 – 3 minutes).

AsiaFlux (https://www.asiaflux.net/) is a scientific community with the aim of developing collaborative research and datasets on carbon, water, and energy cycles in key Asian ecosystems. AsiaFlux has grew from a small network in 1999 to a multi-national science community with more than 400 members from 28 countries (Yamamoto 2005). Currently, there are 109 flux towers in Asia, and more sites are underway. The biomes covered in AsiaFlux range from rainforests near the equator to tundra in the Arctic and Antarctic, and from wetlands near sea level to grasslands at high altitudes, such as the Tibetan Plateau. Most sites have a time resolution of 0.5 hour, while 15 minutes and 1 hour are used for individual sites.

The Atmospheric Radiation Measurement (ARM, https://www.arm.gov/) Program, supported by the U.S. Department of Energy, is a project for atmospheric measurement and modeling. The purpose of the project was to detect processes that affect atmospheric radiation and describe these processes in climate models (Stokes and Schwartz 1994). The quantities measured at these stations included longwave and shortwave radiation, clouds properties, water vapor, other radiation-related quantities, and meteorological variables. These sites had the high temporal resolution of 1 minute.

The Ice and Climate group at the Institute for Marine and Atmospheric Research of Utrecht University (UU/IMAU, https://www.projects.science.uu.nl/iceclimate/) has deployed several Automatic Weather Stations (AWS) on different glaciers around the world (Antarctica, Greenland, Alps, Norway, Iceland, Svalbard), and in different climate regimes. The stations were designed to operate on a long-term basis and measure meteorological and radiation variables in remote regions under harsh weather conditions. The main purpose of these stations is to detect the energy balance in these regions in view of climate change and, sea-level variation. The stations from the IMAU project have time resolutions of 1 and 2 hours.

Denmark launched the Programme for Monitoring of the Greenland Ice Sheet (PROMICE, https://www.promice.dk/) to detect variations in the mass balance of the Greenland ice sheet. Several weather stations were established on the ice sheet to provide filed data for modeling and validation. The weather stations were equipped with CNR1 or CNR4 instruments to measure radiation data with a time resolution of 10 minutes.

267   The National Tibetan Plateau Data Center (TPDC, http://data.tpdc.ac.cn) has integrated and released

268   various scientific data from the Qinghai-Tibet Plateau and surrounding regions. Integrated data resources

269   include the atmosphere, cryosphere, hydrosphere, and energy balance. Among these data sources, there

270   are various published ground measurements. We selected several stations in the Heihe Basin (Liu et al.

271   2018), Haihe Basin (Liu et al. 2013b), and Qinghai-Tibet Plateau (Ma et al. 2020b). The time resolutions

272   of these stations were 10 minutes, 30 minutes and 1 hour, respectively.

273   Some stations from various flux networks overlapped, and we curated observations with extended

274   time series and heightened time resolution. Attaining high model accuracy necessitates superior in situ

275   measurements, necessitating rigorous quality assessment. Initially, adjacent stations potentially causing

276   interference were removed, alongside the manual elimination of anomalous observations and

277   discontinuous measurements. Subsequently, the collection sites were strategically dispersed globally.

278   Fig.2 depicts a histogram illustrating the distribution of land cover types and climate zones across the

279   sites. Each land cover type was accounted for, and additional sites encompassing water bodies were

280   incorporated to estimate LST for inland water. The stations were dispersed across five distinct climate

281   zones, with a higher concentration in temperate and continental climates. Importantly, we meticulously

282   gathered data from numerous high-latitude stations within a polar climate to address substantial

283   estimation uncertainties in the area.
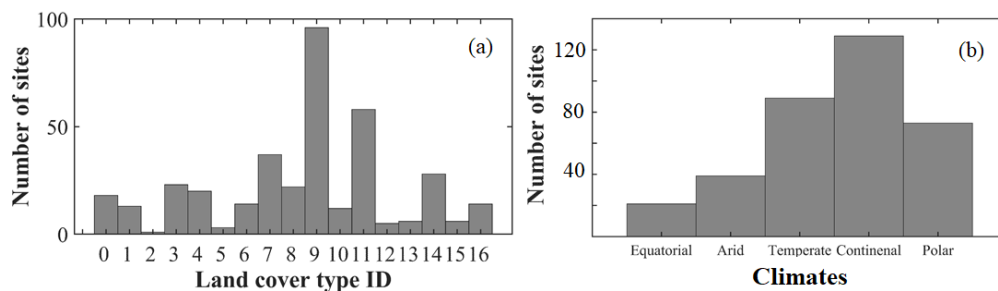
284

285   Fig.2 Land cover types (a) and climate zones (b) of sites (The land surface type represented by the x-axis in (a) refers to the
286   legend in Fig.1

287

288

3 Methods

290 The study's comprehensive framework is depicted in Fig.3. Initially, the in situ LST and remote

291 sensing data underwent preprocessing and pairing. Subsequently, the data pairs were randomly divided

292 into two segments: one for model training and validation, while the other served as an independent dataset

293 for model evaluation. The XGBoost algorithm was employed to sequentially develop models for

294 instantaneous and daily mean LST, while also conducting parameter tuning. The estimated all-weather

295 instantaneous LST served as an input for the daily mean LST model. Ultimately, the optimal models

296 underwent separate evaluation and comparison with alternative products.

297

298 Fig.3 Flowchart of the XGBoost algorithm for all-weather instantaneous and daily mean LST estimation.

299 **3.1 Data Preprocessing**

300 **3.1.1 In situ instantaneous LST**

301 The in situ LST in this study was calculated from surface broadband emissivity and in situ upwelling

302 and downwelling longwave radiation, according to Stefan–Boltzmann's law, as follows:

$$T_S = \left(\frac{F_{up} - (1-\varepsilon)F_{dn}}{\sigma\varepsilon}\right)^{\frac{1}{4}}, \tag{1}$$

304 where T_S represents the in situ LST, F_{up} is the upwelling longwave radiation, and F_{dn} is the

305 downwelling longwave radiation, ε is surface broadband emissivity, and σ is the Stefan-Boltzmann

306 constant (5.67×10^{-8} W/m^2/K^4).

307 Surface broadband emissivity was acquired from the GLASS BBE product through nearest

308   interpolation to derive daily values. F_{up} and F_{dn} were derived from in situ measurements. Due to

309   varying observation intervals across different networks, spanning from 1 minute to 1 hour, a linear

310   interpolation method was applied to determine the in situ LST corresponding to the MODIS satellite

311   observation time.

312   **3.1.2 Daily mean LST**

313   To construct a daily mean LST model, in situ daily mean LST and ERA daily mean LST are required.

314   Once the instantaneous LST from in situ measurements was obtained, the daily mean in situ LST was

315   calculated according to Eq. (2). The ERA daily mean LST was obtained using Eq. (3).

$$LST_{DS} = \frac{1}{n}\sum_{i=1}^{n} LST(i)_{IS} \tag{2}$$

$$LST_{DE} = \frac{1}{24}\sum_{i=1}^{24} LST(i)_{IE} \tag{3}$$

318   LST_{DS} and LST_{DE} represent the daily mean in situ LST and ERA daily mean LST respectively, and

319   n is the count of the in situ measurements per day. LST_{IS} and $LST(i)_{IE}$ are the instantaneous in situ

320   LST values calculated from Eq. (1) and ERA LST, respectively. If the in situ measurements were

321   incomplete in a day, the record for that day was not used.

322   One traditional daily mean LST method, which was retrieved from the official MODIS Aqua LST

323   for both daytime and nighttime (Williamson et al. 2014), was used for comparison. The equation can be

324   expressed as follows:

$$LST_{DM} = 0.5 * LST_{AD} + 0.5 * LST_{AN} \ , \tag{4}$$

326   where LST_{DM} represents the retrieval of the daily mean LST, and LST_{AD} and LST_{AN} represent

327   the daytime and nighttime LST, respectively from the official MODIS Aqua LST.

328

329   **3.1.3 Data normalization**

330   Due to discrepancies in spatial and temporal resolutions among the utilized products, preprocessing

331   was conducted. Albedo and BBE had an 8-day temporal resolution, and the daily data were acquired

332   through nearest interpolation. DSR and ERA LST were adjusted to a spatial resolution of 1 km via the

333   nearest-neighbor method. The ERA LST, with a temporal resolution of 1 hour, was interpolated linearly

334   to obtain the reanalysis LST at the satellite observation time. Matching of in situ measurements and

335 satellite data was performed based on coordinates from MOD03/MYD03 products.

336 **3.2 Developing the estimation algorithm**

337 Extreme Gradient Boosting (XGBoost) is an effective and scalable gradient boosting

338 implementation introduced by Chen and Guestrin (2016). It amalgamates multiple classification and

339 regression trees to create a robust learner. In regression, the initial tree is constructed based on split

340 features, followed by the creation of subsequent trees to capture residuals from the preceding ones.

341 Additional trees are iteratively generated until they meet the stopping criteria. Notably, the regression

342 trees within XGBoost are interrelated, progressively diminishing the residuals of predictions with new

343 trees. The ultimate prediction is derived by aggregating scores from each tree.

344 In contrast to the random forest method, which also employs decision trees (Breiman 2001),

345 XGBoost operates in parallel. Its algorithm design incorporates column blocks for parallel learning,

346 cache-aware access, and facilitates out-of-core computation, substantially boosting computational

347 efficiency. Owing to XGBoost's notable efficiency and precision, many studies in remote sensing have

348 adopted this algorithm for regression tasks (Kim et al. 2021; Liu et al. 2021; Zhang et al. 2023). In this

349 research, XGBoost was implemented using the Scikit-learn package in Python. Experiments were

350 performed on a computer equipped with a 3.60 GHz CPU and 64 GB RAM, utilizing the same dataset

351 and features. Detailed hyperparameters are elucidated in Section 3.3.

352 **3.3 Model development**

353 The dataset for 2002-2018 were compiled at a global scale. Samples from 238 sites were randomly

354 chosen for model training. The remaining samples from 77 sites were used as independent dataset for the

355 model validation. The features used to construct the instantaneous LST model, included MODIS TOA

356 observations, ERA LST, DSR, LWDN, albedo, and geolocation data. MODIS TOA observations were

357 used to describe the contributions of shortwave and longwave radiation to the LST, which is greatly

358 changed with solar radiation influenced by clouds. Hence, DSR was used to reflect the effect of solar

359 radiation on the LST (Zeng et al. 2018). Longwave radiation is less affected by the atmosphere, has a

360 certain penetration, and has a close correlation and interaction with the LST during the daytime and

361 nighttime. In this study, the LWDN was used to reflect the effect of thermal infrared radiation on LST.

362 LST is also influenced by land cover types, and broadband albedo was used to represent land surface

363   characteristics. In addition, geolocation information, such as solar angles, view angles and height, also

364   affects LST retrieval from satellites. All the input variables were all-weather conditions with high

365   resolution. In addition, ERA LST can provide all-weather LST, but with coarse resolution (0.1°). It was

366   considered as a background field and, provided an initial value for the model. After the instantaneous

367   model was constructed, the daily mean model was developed. Research has confirmed linear or nonlinear

368   relationships between the daily mean LST and instantaneous LSTs for polar orbiting satellites (Duan et

369   al. 2014; Xing et al. 2021). Hence, the instantaneous retrieval of all-weather LST data was used in the

370   daily LST model. In addition, the ERA daily LST rather than the ERA LST was used as the initial value

371   in the daily LST model. Except for these two variables, the inputs of the two models were the same.

372   Specifically, the daily mean LST finally retrieve from the average of multiple observations in one day.

373   Model tuning was performed to prevent over-fitting of the models. Several hyper-parameters in

374   XGBoost needed to be tuned, including the number of gradient boosted trees (n_estimators), maximum

375   depth of trees (Max_depth), minimum sum of weights of all observations required in a child

376   (Min_child_weight), minimum loss reduction required to make a split (gamma), fraction of observations

377   to be randomly samples for each tree (subsample), fraction of columns to be randomly sampled for each

378   tree (Colsample_bytree). Lambda and alpha represent the regularization of the weights in XGBoost,

379   which can improve the speed performance. A random search combined grid search was used to tune the

380   model. Table 2 presents the candidate values of the random search and the final settings for the two LST

381   models.

382

Table 2. Candidate values and selected values of hyper-parameters in XGBoost

Hpyer-parameter	Candidate values	Selected values	
	(start, end, step)	Instantaneous model	Daily model
n_estimators	50,401,10	160	140
Max_depth	1,10,1	9	9
Min_child_weight	1,10,1	5	6
gamma	0,1,0.1	0.8	0.5
subsample	0.1,1,0.1	1	1
Colsample_bytree	0.1,1,0.1	0.8	0.8
lambda	0.1, 2, 0.1	0.6	1.4
alpha	0.1, 2, 0.1	1.6	1.19

383

384   **3.4 Evaluation approaches**

385   In this study, validation from training and independent datasets of separated ground measurements

386   was used to evaluate the instantaneous and daily mean LST models. A widely used ten-fold cross

387   validation (10-CV) method was used to evaluate the stability of the models. Then, model performance

388   was assessed for different weather conditions, and observation times. In addition, time series of

389   individual sites and spatial distribution at regional and global scales were chosen to further demonstrate

390   the effectiveness of the developed models. Finally, the proposed framework and generated products were

391   compared with those of previous studies and products.

4 Results

4.1 Model training and validation

In general, 70% of the dataset was used for the model training. The remaining dataset was used for model adjustment and validation, and was identified as training result. Independent validation and 10-CV results were used to evaluate the models. Fig.4 and Fig.5 show the accuracies of the instantaneous and daily mean LST models, respectively. From the scatter density plots, all the validation results for both the instantaneous and daily models are close to the 1:1 line, with R^2 values ranging from 0.974 to 0.990. The Root Mean Squared Error (RMSE) of the training and validation results were 2.413 K and 2.787 K for the instantaneous model, and while 1.758 K and 2.175 K for the daily mean LST model. Both models showed high accuracy in model training and validation, with no obvious overfitting. The 10-CV method is also used to comprehensively validate the models and the results of both models are also satisfactory, with RMSEs =2.421 K and 1.808 K for the instantaneous and daily mean LST models, respectively. Overall, the validations from the independent dataset and 10-CV results show acceptable accuracy and robustness of the two models. Both models are robust. The daily mean LST model show a higher accuracy than the instantaneous LST model. Probably because the daily mean LST is obtained by averaging multiple observations in one day, which reduces the uncertainty. In addition, some daily inputs (daily mean in situ LST and ERA LST) used in the daily model have less uncertainty than instantaneous observations.
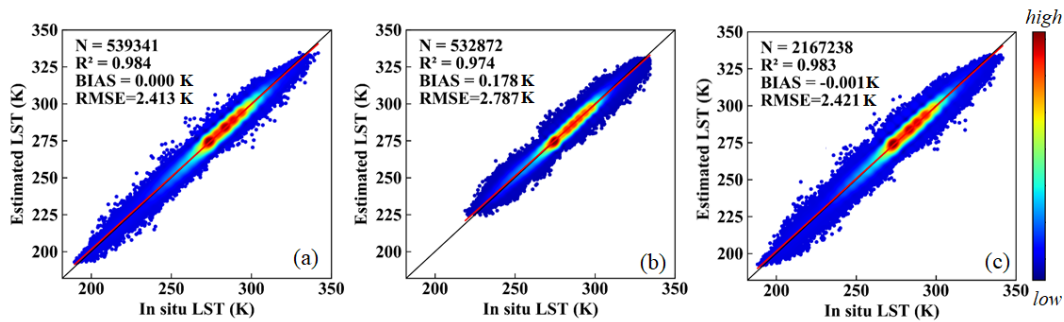
Fig.4 The (a) training, (b) independent validation and (c) 10-CV results of the instantaneous LST model

414
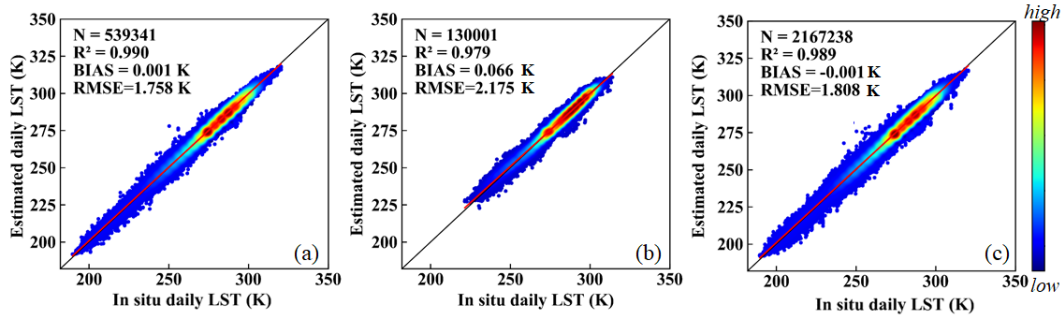
415 Fig.5 The (a) training, (b) independent validation and (c) 10-CV results of the daily mean LST model

416   In addition, we further verify the model performance under different conditions using an

417 independent dataset. Table 3 presents the validation results for different observation times and satellites

418 for the instantaneous model. The RMSEs are 3.03 K and 2.67 K for daytime and nighttime data

419 respectively. The accuracy of nighttime data is higher than that of daytime data. It probably because of

420 the absence of differential solar heating and higher spatial-temporal heterogeneity in daytime (Duan et

421 al. 2019; Liu et al. 2023). In addition, the LST value during the daytime is higher than that during

422 nighttime, which results in a higher RMSE value. For the validation of the MOD and MYD satellites,

423 the RMSE of the MOD is nearest to that of the MYD. We further verify the accuracy in the presence and

424 absence of clouds; the density plots are shown in Fig.6. The accuracy under clear-sky conditions was

425 relatively higher with an RMSE= 2.614 K, whereas the RMSE is 2.931 K under cloudy-sky conditions.

426 More effective observation information and higher accuracy of inputs under clear-sky conditions, result

427 in a higher accuracy of clear-sky estimation. This phenomenon is also present in other studies (Duan et

428 al. 2023; Ma et al. 2024). Furthermore, to explore whether clouds have an effect on daily mean LST

429 retrieval, we calculate the accuracy under different cloud proportions, as shown in Table 3. The results

430 show that with the RMSE values increasing slightly as the proportion of cloudy-sky observations

431 increased. This demonstrates that the cloud contamination has a limited impact on the daily mean LST

432 estimation in the proposed method.

433 Table 3. Validation for different observation times, satellites and weather condition of instantaneous the model, and the

434 proportion of cloudy-sky MODIS observations of the daily LST model

	Groups	R^2	RMSE (K)	Bias (K)
	Daytime	0.960	2.99	0.30
Instantaneous LST model	Nighttime	0.980	2.61	0.05
	MOD	0.980	2.80	0.19

	MYD	0.980	2.82	0.17
Daily LST model	0-30	0.980	2.01	-0.07
(Proportion of cloudy	30-60	0.980	2.14	-0.16
MODIS observations %)	60-100	0.980	2.26	-0.04

435
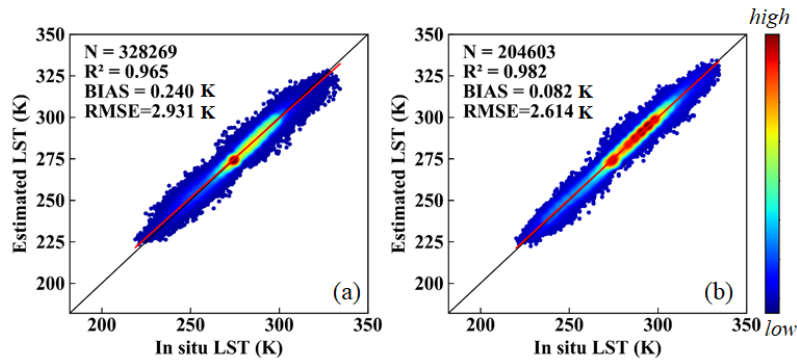
436

437   Fig.6 Validation under (a) cloudy-sky conditions and (b) clear-sky conditions

438 **4.2 Validation and assessment**

439   **4.2.1 Evaluation across individual sites**

440   The validation of the instantaneous and daily mean LST for individual sites is shown in Fig.7. The

441 color of the circles indicates the increasing level of errors. RMSEs rank from 1.16 to 4.90 K for

442 instantaneous LST and 0.89 to 3.96 K for daily mean LST. The corresponding histograms show that the

443 accuracy of nearly 75% of sites is below 3 K and 2.5 K for instantaneous and daily mean LST,

444 respectively. Stations distributed in the continental United States with intensive LST monitoring

445 generally have higher accuracy. High accuracy is also observed at stations in Alaska and Greenland,

446 whereas a relatively lower accuracy is observed in the Antarctic. In Europe, most stations perform well,

447 with the exception of some stations in the east. The stations in Asia are relatively discrete with relatively

448 lower accuracy for individual sites in western China, which is probably due to the high elevation and

449 complex terrain (Jia et al. 2023). In addition, several stations distributed in Australia, Africa, and South

450 America also perform well in both models. In general, the results indicate a satisfactory predictive ability

451 of both instantaneous and daily mean LST models at most individual sites.

452

453
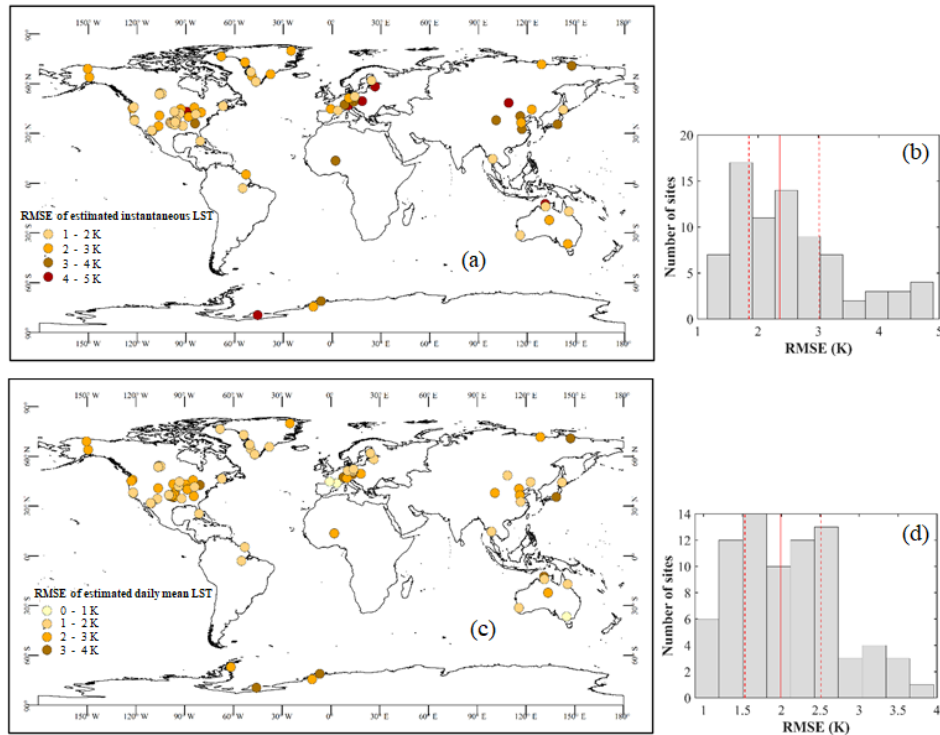
454

455   Fig.7 Validation of individual sites for instantaneous LST (a), daily mean LST (c) and their corresponding histograms (b, d)

456   **4.2.2 Evaluation across land cover types and elevation**

457   LST is closely related to land cover types. The validation results for different land cover types are

458 presented in Table 4. The results indicated that the data had high accuracies for most land cover types.

459 For instantaneous LST, the RMSEs of most vegetation types were below 3 K, except for shrublands with

460 an RMSE of 3.04 K. Among the vegetation types, cropland had an outstanding RMSE of 2.55 K. The

461 accuracies of vegetation types for daily mean LST were higher than that of instantaneous LST, with

462 RMSEs of approximately 2 K, except for shrublands with an RMSE of 2.55 K. The accuracy in water

463 bodies was also satisfactory, with RMSEs of 2.43 and 2.04 K for instantaneous and daily mean LST,

464 respectively. For both models, the accuracy of instantaneous and daily mean LST in snow/ice with RMSE

465 of 2.94 and 2.35 K, respectively were notably improved compared with that found in our previous study

466 (Li et al. 2021). This is probably due to the higher number of samples from high latitudes, which

467 improved the model robustness in snow/ice. However, the accuracy for urban and barren areas was

468 relatively low. This is likely due to the high heterogeneity of urban areas, high albedo and low specific

469 heat capacity of barren land (Duan et al. 2017a). In general, for different land cover types, the daily mean

470 model showed higher accuracy than the instantaneous model, and both models had acceptable accuracy.

471 In addition, we summarized the accuracy of the different elevation ranges in Table 5. The results indicate

that elevation has an impact on LST retrieval accuracy. The relatively poor accuracy at high elevations

is probably due to the harsh natural environment and complex terrain, which was also reflected in another

study (Zhao et al. 2019).

Table 4. Validation of instantaneous and daily LST models for various land cover types

	Instantaneous LST model			Daily mean LST model		
	R^2	RMSE (K)	Bias (K)	R^2	RMSE (K)	Bias (K)
Forest	0.941	2.82	0.11	0.960	2.08	-0.11
Shrublands	0.980	3.04	-1.05	0.980	2.55	-0.85
Savannas	0.960	2.74	0.12	0.980	2.13	0.24
Grassland	0.960	2.65	0.12	0.960	2.02	0.06
Wetland	0.980	2.87	-0.86	0.980	2.19	-0.35
Cropland	0.960	2.55	-0.05	0.960	2.22	0.06
Urban	0.774	3.76	0.4	0.883	2.51	-0.44
Snow	0.941	2.94	0.77	0.960	2.35	0.69
Barren	0.941	3.8	0.95	0.960	3.53	0.85
Water	0.960	2.43	-0.34	0.980	2.04	-0.22

Table 5. Validation of the instantaneous and daily mean LST models for different elevations

	Instantaneous LST			Daily mean LST		
Elevation (m)	R^2	RMSE (K)	Bias (K)	R^2	RMSE (K)	Bias (K)
<500	0.960	2.63	-0.06	0.980	2.14	0.12
500-1000	0.980	2.85	0.60	0.980	2.16	-0.35
1000-2000	0.980	3.25	0.39	0.980	2.29	-0.41
>2000	0.941	3.79	-0.83	0.941	2.74	1.23

4.2.3 Comparison with other products

Official MODIS and ERA LST data were used for comparison with our LST products. Fig.8 presents

the accuracy of ERA LST (RMSE = 4.048 K) and official MODIS LST (RMSE = 3.583 K), both of

which were lower than the accuracy of the estimated LST proposed in this study (RMSE = 2.787 K,Fig.4).

Furthermore, we noted that the official MODIS LST data had several abnormal points (Fig.8.(b)). The

polar regions (Antarctica and the Arctic pole) were verified separately from the other regions, as shown

in Fig.9. The results indicate that the majority of outliers were from stations located in Antarctica and the

Arctic pole (Fig.9.(b)), probably because of cloud contamination. Owing to the spectral similarities

between the ice and snow, the misjudgment of clouds leads to cloud top temperatures rather than LST

(Liu et al. 2010; Østby et al. 2014). In contrast, the proposed method was unaffected by cloud

contamination (Fig.9 (a)).
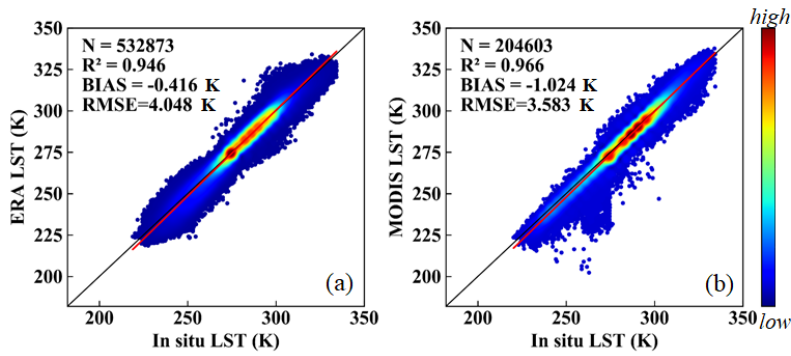
489
490   Fig.8 Density plots of (a) ERA LST and (b) MODIS clear-sky LST
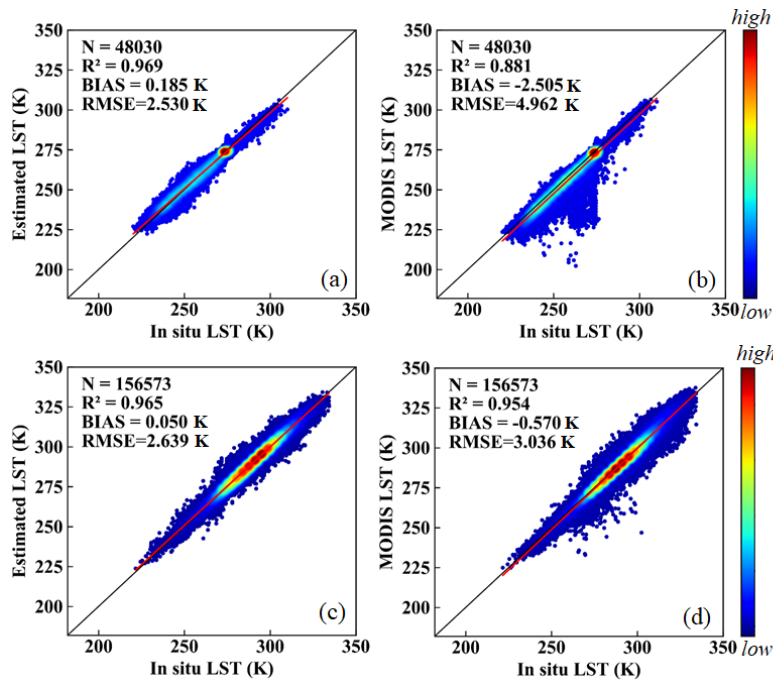
491
492 Fig.9 Density plots of estimated instantaneous clear-sky LST (a, c) and MODIS LST (b, d) in polar regions (first row) and
493   other regions (second row)

494   The daily mean LST from the ERA LST from Eq. (3), and official MODIS LST from Eq. (4)) were

495 used for comparison (Fig.10). The ERA daily LST had an acceptable accuracy, with an RMSE of 2.988

496 K. The RMSE of the daily mean official MODIS LST was 3.105 K. The accuracy of the MODIS official

497 LST was relatively lower compared to what was reported in a previous study. This may be due to the

498 large uncertainty in the official MODIS LST in polar regions. When removing the observations in polar

499 regions, the accuracy improved with an RMSE of 2.799 K, similar to the result in previous studies

500 (Williamson et al. 2014; Xing et al. 2021). The proposed method in this study has a higher accuracy than

501 the daily mean LST from ERA and official MODIS LST, with an RMSE of 2.175 K at the global scale

502 (Fig.4.(b)). Moreover, the daily mean LST obtained from official MODIS LST is only suitable under

503 clear-sky conditions, whereas the daily mean LST obtained in this study was for all-weather conditions.
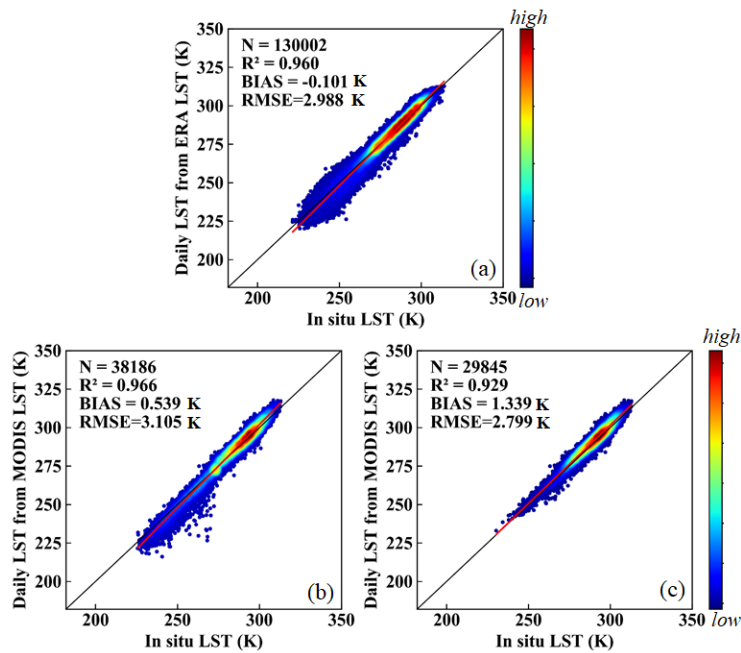
Fig.10 Density plots of (a) ERA daily mean LST and (b) official MODIS daily mean LST (c) official MODIS daily mean LST except polar regions

4.3 Spatiotemporal performance

To further evaluate the temporal performance of the estimated LST, four in situ LST measurements from different latitudes in 2010 were evaluated. Initially, instantaneous LST was examined separately for daytime and nighttime, and MODIS LST was provided for comparison (Fig.11). The RMSE values of the comparable accuracy with MODIS LST. The nighttime LST was more concentrated than the daytime LST. The estimated LST curves are in good agreement with the in situ LST and MODIS LST curves, but are more continuous than the curve of MODIS LST. Discontinuities observed at high-latitudes stations (latitude:79.835, longitude: -25.166) were due to polar day and night phenomena. The daily mean LST was also examined using in situ LST measurements (Fig.12). The daily mean LST retrieved from MODIS official LST were used for comparison. The results indicated higher accuracy and better consistency compared to instantaneous LST. The estimated daily LST also depicted more complete curves than the daily mean LST from MODIS LST, and captured the seasonal variation trends. The results demonstrate that both the estimated instantaneous LST and daily mean LST can correctly reflect the temporal variations in LST.
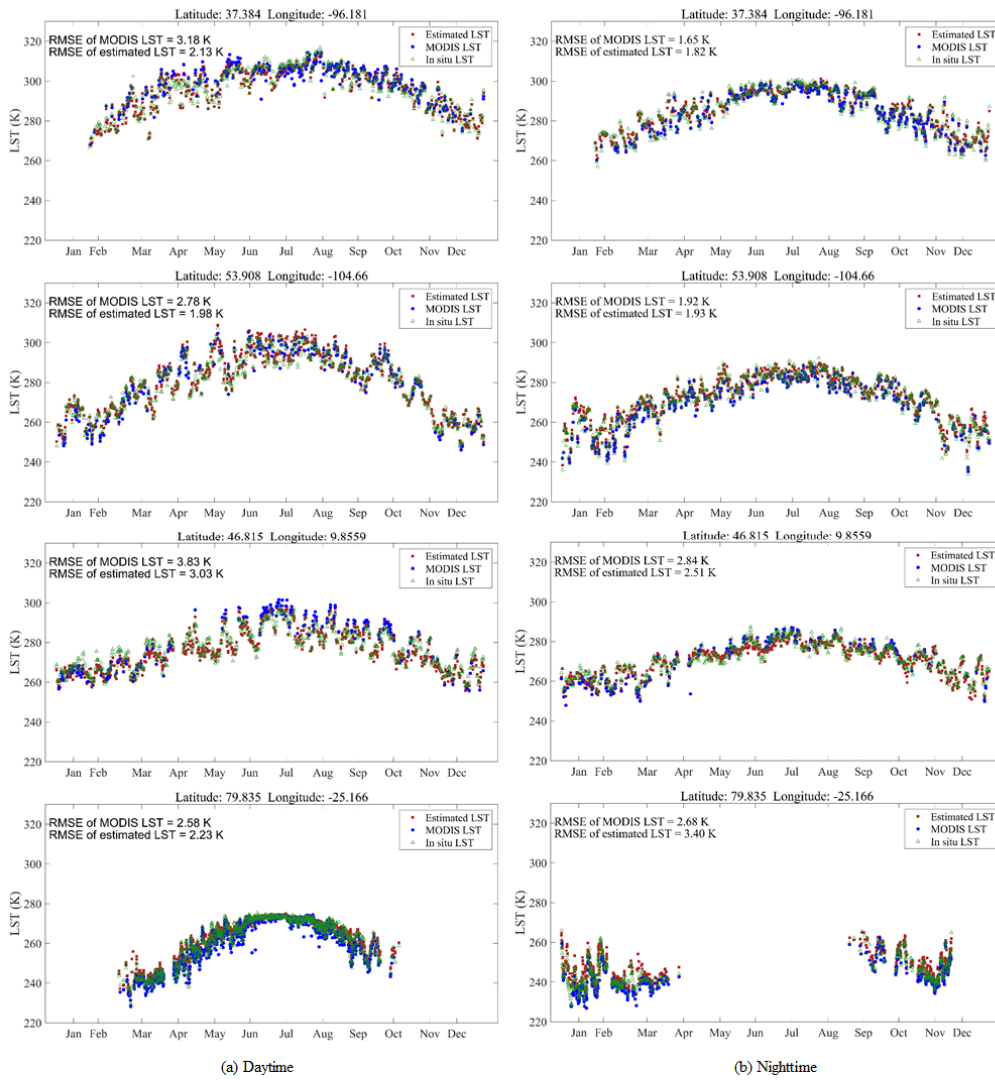
521
522   Fig.11 Time series of the estimated instantaneous LST, MODIS LST, and in situ LST at four sites from different regions in

523   2010: (a) daytime, (b) nighttime.
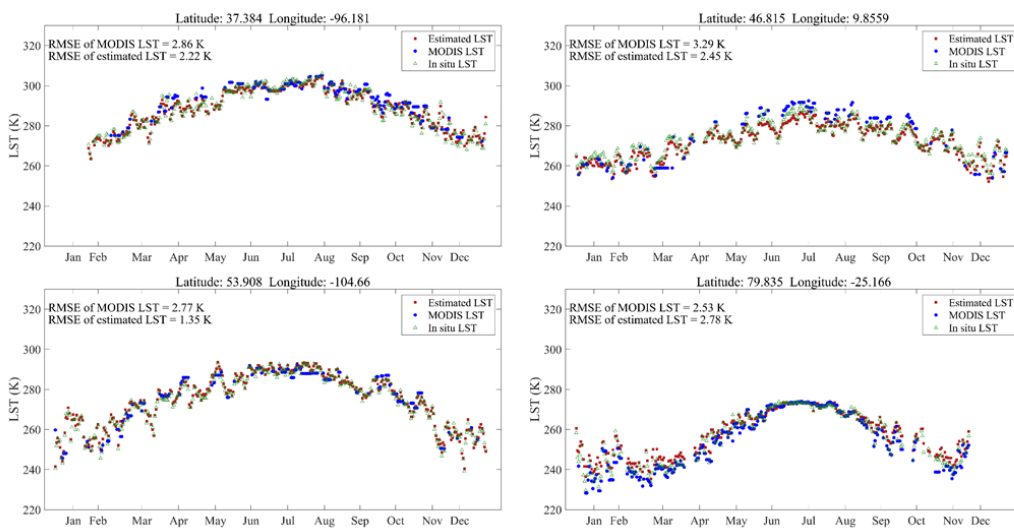
524
525   Fig.12 Time series of the estimated daily mean LST, daily mean LST retrieved from MODIS LST, and in situ LST at four

526   sites from different regions in 2010

527   To further evaluate the spatial performance of the proposed methods, regional distributions and

528   global maps were compared. Fig.13 and Fig.14 present the spatial details of the estimated instantaneous

529   LST and daily mean LST from tiles H10V04, H23V04 and H24V05. One of the grids, H24v05, is located

530   on the Tibetan Plateau and contains mountainous terrain. The instantaneous and daily mean LST from

531   ERA LST and MODIS LST were used for comparison. MODIS LST had missing values caused by cloud

532   contaminants for both instantaneous and daily mean LST, while our method achieved spatially

533   continuous estimation. In addition, the estimated LSTs had spatial patterns similar to those of MODIS

534   LST under clear-sky conditions. Compared with the ERA LST, which was used as the model input, our

535   results showed more spatial details and corrected the underestimation in some regions. In particular, the

536   results of H24v05 reflect that the estimated LST has mountainous details. Demonstrates that our approach

537   is equally applicable to mountainous regions with high heterogeneity. The spatial details of the daily

538   mean LST show similar conclusions (Fig.14). Overall, for both instantaneous and daily mean LST, the

539   proposed methods executed the spatially contiguous LST and, depicted the spatial LST details and

540   variations.
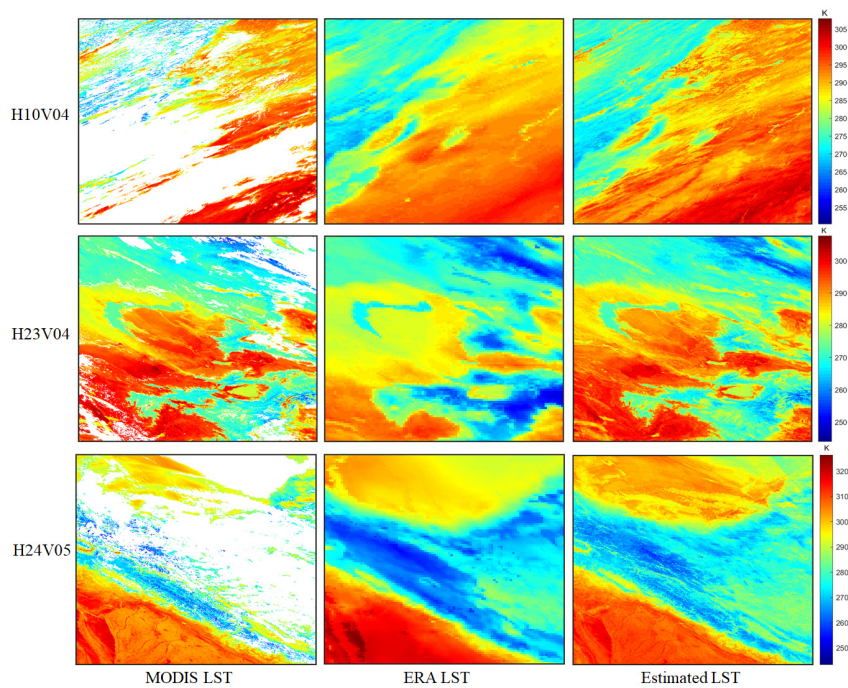
541

542   Fig.13 Spatial details of the MODIS LST, ERA LST and estimated instantaneous LST of three tiles, H10V04 (the first row),

543   H23V04 (the second row) and H24V05 (the third row) from the ninetieth day in 2010

544

MODIS daily mean LST   ERA daily mean LST   Estimated daily mean LST
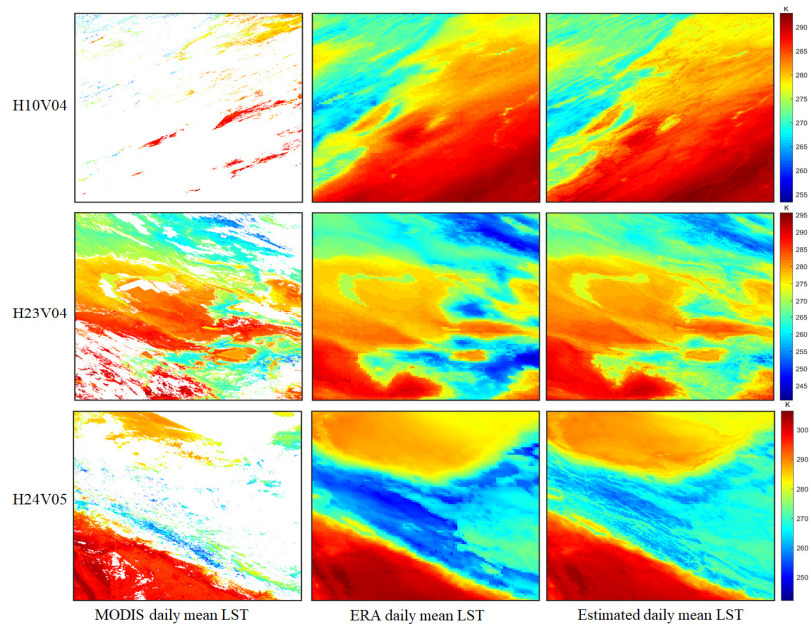
Fig.14 Spatial details of the daily mean LST retrieved from MODIS LST, ERA LST and estimated daily mean LST of three tiles H10V04 (first row) , H23V04 (the second row) and H24V05 (the third row) from the ninetieth day in 2010.

Urban heat island effect is one of the main applications of LST data. To further assess the spatial details of the estimated all-weather LST and the potential of urban heat island applications, we selected four cities in different regions around the globe. And demonstrated the estimated LST in conjunction with the boundary of urban regions extracted by using global artificial impervious area data (Li et al. 2020), as shown in Fig.15. The figure shows that the built-up areas of four cities present higher LST than the periphery, and confirms that our estimated all-weather LST can capture the urban heat island phenomenon and present relevant details.
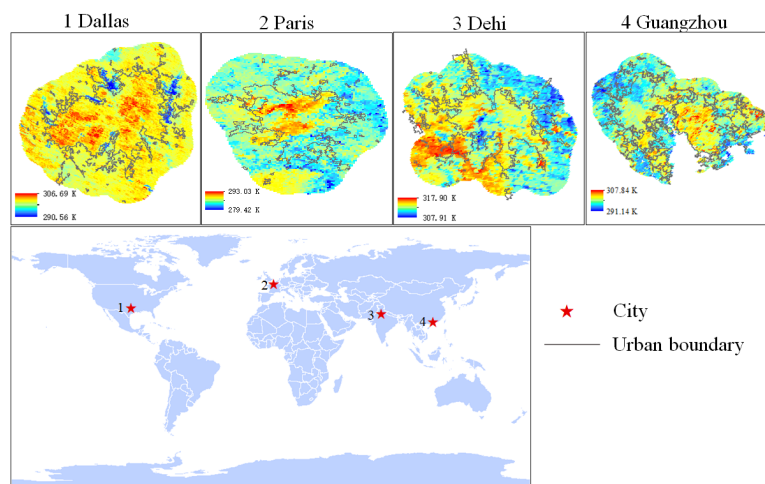
Fig.15 Spatial pattern of the estimated all-weather LST in four representative cities. The black lines are the boundary of urban regions extracted by using global artificial impervious area data.

In addition, Fig.16 and Fig.17 show the estimated instantaneous and daily mean LST at the global

scale on Days 90 and 270 of 2010. The instantaneous and daily mean LST from MODIS LST are shown for comparison. The estimated instantaneous and daily LST had similar spatial patterns to the corresponding LST from MODIS. All of the results reflected broad spatiotemporal variations. For instance, LSTs were relatively higher at middle and low latitudes, and lower in the Arctic and Antarctic. The instantaneous LST exhibited a larger range than the daily mean LST. In addition, the proposed method achieved the all-weather LST retrievals. For instantaneous LST (Fig.16), a small number of gaps in tropical regions were due to the polar-orbiting satellite configuration. The daily mean LST (Fig.17) was spatially continuous. Overall, the proposed instantaneous LST and daily mean LST perform well on a global scale.
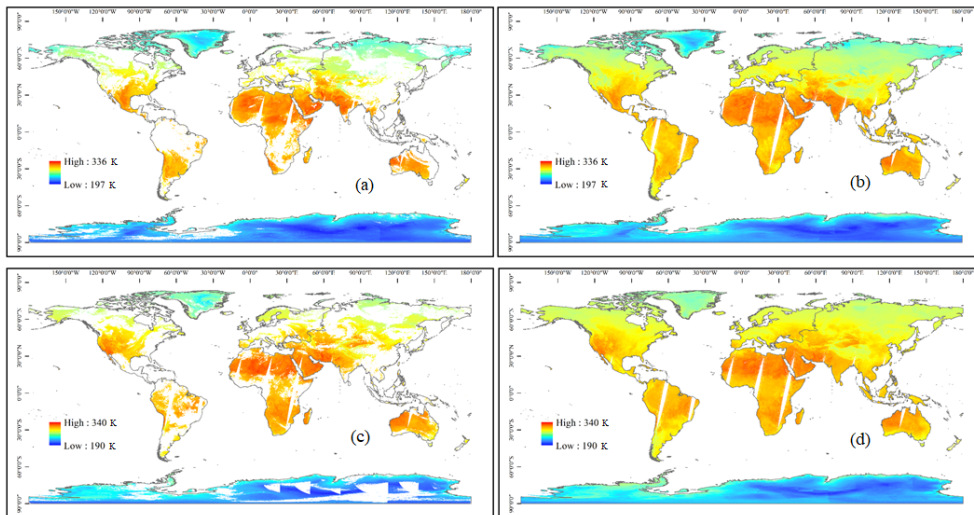
Fig.16 Spatial patterns of MODIS LST (a, c) and estimated instantaneous LST (b, d) at a global scale on the Days 90 (first row) and 270 (second row) of 2010.
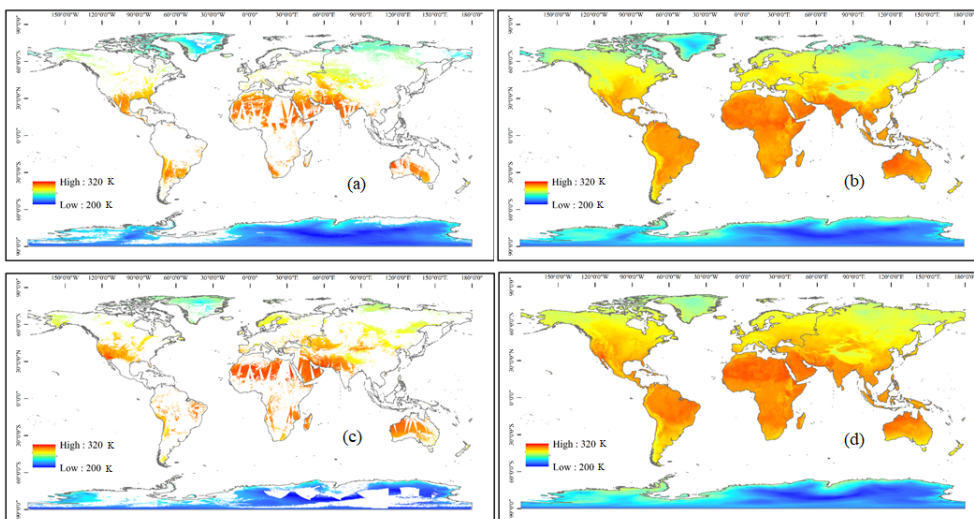
Fig.17 Spatial patterns of daily mean LST retrieved from (a, c) MODIS LST and (b, d) estimated daily mean LST at a global scale on Days 90 (first row) and 270 (second row) of 2010.

5 Discussion

Although several LST satellite products have been published, they are missing data under cloudy-sky conditions. Existing research on all-weather LST has mostly been conducted at the regional scale. This study proposes a highly accurate and efficient algorithm to retrieve all-weather LST at a global scale from multi-source data, including MODIS TOA, surface radiation, reanalysis and in situ data. An all-weather daily mean LST algorithm was also proposed. Both the estimated instantaneous and daily mean LST had acceptable accuracy. In addition, it performs well based on independent ground measurements and space-time verification.

5.1 Effect of introducing MODIS TOA information and ERA LST

In view of the complexity of global climate conditions, and to include more information to estimate the all-weather LST, we introduced MODIS TOA data on the basis of using surface variables. In addition, since the Global Land Data Assimilation System (GLDAS) LST used in previous studies did not have global coverage (the Antarctica region was missing), we introduced the ERA LST in this study, which not only has global coverage, but also has a higher spatio-temporal resolution (0.1°,1 h). We conducted experiments with combinations of different features, to clarify the effect of introducing MODIS TOA information and ERA LST under different weather conditions. A comparison of the removal of ERA LST and MODIS TOA data in the models is shown in Table 6. The results show that when the ERA LST and TOA data were removed, the accuracy of the model was greatly reduced. The RMSEs increased from 2.787 to 3.536 K and 3.466 K when ERA LST and TOA data were removed, respectively. However, the accuracy changes in the two feature combinations under different weather conditions were significantly different. When ERA LST was eliminated, although the accuracies of both weather conditions were reduced, the RMSE increase for cloudy sky (0.95 K) was significantly greater than that for clear sky (0.09 K). When the TOA data was removed, the results were the opposite. The accuracy of clear-sky LST estimation decreased significantly. Overall, introducing MODIS TOA information and ERA LST significantly improved the model accuracy. In addition, it can be inferred that ERA LST provides more effective information for cloudy-sky LST estimation, while TOA data contributes more to clear-sky conditions.

Table 6. The accuracy of the independent dataset with different feature combinations for the instantaneous LST model

Feature combination	All-weather			Clear sky			Cloudy sky		
	RMSE (K)	Bias (K)	R^2	RMSE (K)	Bias (K)	R^2	RMSE (K)	Bias (K)	R^2
All features	2.787	0.178	0.974	2.614	0.082	0.982	2.931	0.240	0.965
No ERA LST	3.536	-0.012	0.959	2.730	-0.14	0.980	3.950	0.07	0.941
No Toa data	3.466	0.335	0.960	3.620	0.21	0.960	3.360	0.41	0.960

5.2 Effect of station density on the model accuracy

To further evaluate the station density on the model accuracy, experiments were conducted with station density and regional validation. Firstly, the stations were reduced randomly in the training dataset, and the model performance was evaluated based on the same test samples. The accuracies of the instantaneous and daily mean models were shown in the Table 7. The result shows that the accuracy of both models decreases as the number of stations in the training sample decreases. When the number of stations in the training sample is reduced from 238 to 158, the RMSE of the instantaneous model increases from 2.787 K to 2.988 K, and the RMSE of the daily model increases from 2.374 K to 2.479 K. The experiment indicates the model accuracy is affected by the station density, but to a limited extent when there is a sufficient amount of samples. It may be that the long time series of station data used in the experiment provided relatively sufficient samples.

Table 7.The training and testing accuracy of instantaneous and daily mean LST with the number of stations decreasing in the training model.

training stations	training samples	instantaneous model			daily mean model		
		RMSE (K)	Bias (K)	R^2	RMSE (K)	Bias (K)	R^2
238	1797803	2.787	0.178	0.974	2.374	0.100	0.978
218	1609953	2.828	0.203	0.974	2.397	0.121	0.978
198	1420496	2.867	0.211	0.973	2.421	0.116	0.977
178	1327160	2.877	0.243	0.973	2.426	0.140	0.977
158	1072730	2.988	0.239	0.971	2.479	0.160	0.976

5.3 Effect of multiple MODIS observations

In contrast to most studies using MODIS data in sinusoidal projection, we used swath-type MODIS data to estimate daily mean LST in this study. MODIS swath data can provide more observations, particularly at high latitudes. Furthermore, we statistically analyzed the relationship between the daily mean LST model error and MODIS observation frequency. Fig.18 shows that the error decreased with

622 an increase in the MODIS observation frequency. For high-latitude areas with more observations, the

623 model accuracy at high latitudes was improved. This demonstrates the superiority of using MODIS data

624 in swath types with more observations to construct a daily mean LST model.
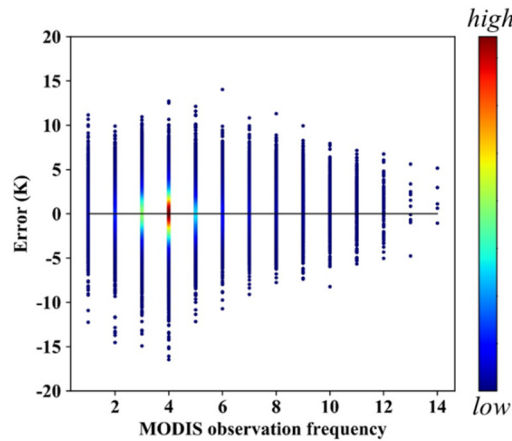
625

626 Fig.18 Density plots of daily mean LST model error with respect to MODIS observation frequency

627 **5.4 Effect of in situ measurements in the model**

628 In contrast to previous studies that used machine learning algorithms, in situ measurements were

629 used to construct the model instead of clear-sky MODIS LST. In situ measurements can obtain the real

630 LST under cloudy-sky conditions, without obtaining the hypothetical LST from clear-sky MODIS LST.

631 In addition, LST from in situ measurements is close to hemispherical LST, or observing the LST from

632 the zenith. In contrast, MODIS LST is a directional LST with view angles ranging from 0° ups to >60°,

633 resulting in a significant thermal radiation directionality (TRD) effect (Cao et al. 2019; Ermida et al.

634 2017). This results in a difference in the LST of the same object at different observation angles.

635 Theoretically, the proposed instantaneous LST weakens the influence of the TRD effect, which was been

636 confirmed in our previous study (Li et al. 2021).

637 **5.5 Effect of the new algorithm on product generation**

638 In previous study, the random forest algorithm (RF) was used to estimate the all-weather LST over

639 the conterminous United States (Li et al. 2021). Although the RF algorithm performs well, the application

640 efficiency needs to be considered for generating global products. Hence, the model accuracy and

641 efficiency were compared using RF and XGBoost. The model accuracies of RF and XGBoost was

642 comparable, with RMSEs of 2.787 K and 2.801 K, respectively (Table 8). However, training the

643 XGBoost model significantly less time, taking up 3.33 minutes compared to 60.01 minutes for RF

training. XGBoost also had outstanding performance in model application. As an example, to produce

100 LST swath-type images, the XGBoost took 8.93 minutes while the RF model took 38.85 minutes

(Table 8). Considering the quantities of swath files at the global scale, XGBoost is a better choice for

long-sequence product generation, with high accuracy and efficiency.

Table 8 Comparison of algorithms of model accuracy and efficiency.

Algorithm	Model accuracy			Model efficiency	
	RMSE (K)	Bias (K)	R^2	Training time(minute)	Application time (minute)
XGBoost	2.787	0.178	0.974	3.33	8.93
RF	2.801	0.196	0.974	60.01	38.85

5.6 Limitations

However, this study has certain limitations. Despite enhancements in LST accuracy on ice and snow

surfaces, accuracy remains comparatively lower in barren and urban areas. Additionally, while the study

aimed to select the highest possible number of representative ground stations for the long-term sequence,

the spatial distribution was non-uniform, potentially impacting the generality of data-driven models.

Furthermore, the accuracy of the high-altitude model was marginally lower, possibly attributed to the

complex climatic environment and topographic conditions. Future investigations could employ advanced

methods, such as deep learning, to develop a more adaptive model incorporating spatial and temporal

information. Moreover, integration with other satellite sensors has the potential to extend the temporal-

spatial resolution and time span of all-weather LST products.

6 Data availability

661

662   The global all-weather LST data at monthly scale from 2000-2020 can be freely downloaded from

663   https://doi.org/10.5281/zenodo.4292068(Li et al. 2024), the daily mean LST on the first day of year 2010

664   is freely available at (Li et al. 2024), all the data will be available at https://glass-

665   product.bnu.edu.cn/dload.html.

666

7 Conclusion

LST is a crucial parameter of the Earth's energy budget, and current LST satellite products are affected by cloud contamination, resulting in missing values. This study attempted to retrieve all-weather instantaneous and daily mean LST at a global scale. A new framework that generating global, long-sequence LST product is proposed. Multiple all-weather datasets from MODIS TOA observations, surface radiation data, geolocation data, reanalysis data, and ground measurements were used to construct the models.

Based on the XGBoost algorithm and multisource data from 2002-2018, all-weather instantaneous and daily mean LST models were successively built. The validation of the independent dataset showed high accuracy. The ten-fold cross validation demonstrated the robustness of the models. For the instantaneous LST model, clear-sky LST showed higher accuracy than cloudy-sky LST, while cloud contamination had limited effects on daily mean LST estimations. Both models performed well for most land cover types and geolocation conditions. The time series for validation at the four sites from different regions was temporally contiguous. The results showed high consistency with in situ measurements and the corresponding official MODIS LST. The spatial distributions of MODIS tiles showed more spatial details than the ERA LST. Global mapping illustrated spatial continuity and similar patterns with instantaneous and daily mean LST from the official MODIS LST data.

Compared with previous products, adding TOA observations effectively improved the accuracy of the instantaneous model, especially under clear-sky conditions. Moreover, multiple effective swath-type observations from the MODIS data significantly improved the accuracy of the daily mean LST model. In contrast to the MODIS and ERA LST, the proposed all-weather method has a higher accuracy and is less affected by cloud contamination, especially at high latitudes. In terms of product generation, XGBoost has higher precision and efficiency compared with RF, and provides effective support for mass data production.

Overall, the proposed models were effective and robust, demonstrating the potential of estimating all-weather instantaneous and daily mean LST from multisource data. The constructed models can be used to generate long-sequence LST products from 2000 to present. The generated product is a 1 km all-weather instantaneous and daily mean LST products at a global scale. It has great significance for studies on climate change, surface energy balance, and many other scientific fields. In the future, new methods

696   involving spatial and temporal information, as well as other satellite sensors, should be considered to

697   expand the spatiotemporal monitoring capabilities of LST products.

698

699 **Declaration of Competing Interest**

700   Author Han Ma is a member of the editorial board of the journal.

701

702 **Acknowledgements**

703   This project was funded by the National Natural Science Foundation of China (No.42301438, No.

704 42090011), the Key Scientific and Technological Project of Henan Province (No.232102321103) and the

705 Project funded by China Postdoctoral Science Foundation (No.23M730941). We gratefully acknowledge

706 the data support from "National Earth System Science Data Center, National Science & Technology

707 Infrastructure of China" (http://www.geodata.cn). The product will also be downloaded at https://glass-

708 product.bnu.edu.cn. We also thank the National Aeronautics and Space Administration team for

709 providing the MODIS products data freely download via the website https://earthdata.nasa.gov/.We also

710 appreciated the ERA5-land reanalysis data from https://cds.climate.copernicus.eu/. Additionally, authors

711 would like to acknowledge the several networks including AmeriFlux, AsiaFlux, ARM, BSRN,

712 FLUXNET, IMAU, PROMICE, TPDC, that provide valuable ground measurements in this study.

Reference

Aires, F., Prigent, C., & Rossow, W.B. (2004). Temporal interpolation of global surface skin temperature diurnal cycle over land under clear and cloudy conditions. *Journal of Geophysical Research: Atmospheres, 109*, 313-331

Auger, M., Morrow, R., Kestenare, E., Sallee, J.B., & Cowley, R. (2021). Southern Ocean in-situ temperature trends over 25 years emerge from interannual variability. *Nat Commun, 12*, 514

Baldocchi, D., Falge, E., Gu, L., Olson, R., Hollinger, D., Running, S., Anthoni, P., Bernhofer, C., Davis, K., Evans, R., Fuentes, J., Goldstein, A., Katul, G., Law, B., Lee, X., Malhi, Y., Meyers, T., Munger, W., Oechel, W., Paw, K.T., Pilegaard, K., Schmid, H.P., Valentini, R., Verma, S., Vesala, T., Wilson, K., & Wofsy, S. (2001). FLUXNET: A New Tool to Study the Temporal and Spatial Variability of Ecosystem–Scale Carbon Dioxide, Water Vapor, and Energy Flux Densities. *Bulletin of the American Meteorological Society, 82*, 2415-2434

Baldocchi, D.D. (2003). Assessing the eddy covariance technique for evaluating carbon dioxide exchange rates of ecosystems: past, present and future. *Glob Chang Biol, 9*, 479-492

Bastiaanssen, W.G., Menenti, M., Feddes, R., & Holtslag, A. (1998). A remote sensing surface energy balance algorithm for land (SEBAL). 1. Formulation. *Journal of Hydrology, 212*, 198-212

Boden, T.A., Krassovski, M., & Yang, B. (2013). The AmeriFlux data activity and data system: an evolving collection of data management techniques, tools, products and services. *Geoscientific Instrumentation, Methods and Data Systems, 2*, 165-176

Breiman, L. (2001). Random forests. *Machine Learning, 45*, 5-32

Cao, B., Liu, Q., Du, Y., Roujean, J.-L., Gastellu-Etchegorry, J.-P., Trigo, I.F., Zhan, W., Yu, Y., Cheng, J., Jacob, F., Lagouarde, J.-P., Bian, Z., Li, H., Hu, T., & Xiao, Q. (2019). A review of earth surface thermal radiation directionality observing and modeling: Historical development, current status and perspectives. *Remote Sensing of Environment, 232*

Chen, B., Huang, B., & Xu, B. (2015). Comparison of Spatiotemporal Fusion Models: A Review. *Remote Sensing, 7*, 1798-1835

Chen, T., & Guestrin, C. (2016). Xgboost: A scalable tree boosting system. In, *Proceedings of the 22nd acm sigkdd international conference on knowledge discovery and data mining* (pp. 785-794)

Chen, Y., Liang, S., Ma, H., Li, B., He, T., & Wang, Q. (2021). An all-sky 1 km daily surface air temperature product over mainland China for 2003–2019 from MODIS and ancillary data. *Earth System Science Data*

Cheng, J., & Liang, S. (2013). Estimating global land surface broadband thermal-infrared emissivity using advanced very high resolution radiometer optical data. *International Journal of Digital Earth, 6*, 34-49

Cheng, J., & Liang, S. (2014). Estimating the broadband longwave emissivity of global bare soil from the MODIS shortwave albedo product. *Journal of Geophysical Research: Atmospheres, 119*, 614-634

Cheng, J., & Liang, S. (2016). Global Estimates for High-Spatial-Resolution

Clear-Sky Land Surface Upwelling Longwave Radiation From MODIS Data. *IEEE Transactions on Geoscience and Remote Sensing, 54*, 4115-4129

Cheng, J., Liang, S., Wang, W., & Guo, Y. (2017). An efficient hybrid method for estimating clear-sky surface downward longwave radiation from MODIS data. *Journal of Geophysical Research: Atmospheres, 122*, 2616-2630

De Jeu, R.A. (2003). Retrieval of land surface parameters using passive microwave remote sensing. *PhD diss., Vrije Universiteit Amsterdam*

Driemel, A., Augustine, J., Behrens, K., Colle, S., Cox, C., Cuevas-Agulló, E., Denn, F.M., Duprat, T., Fukuda, M., Grobe, H., Haeffelin, M., Hodges, G., Hyett, N., Ijima, O., Kallis, A., Knap, W., Kustov, V., Long, C.N., Longenecker, D., Lupi, A., Maturilli, M., Mimouni, M., Ntsangwane, L., Ogihara, H., Olano, X., Olefs, M., Omori, M., Passamani, L., Pereira, E.B., Schmithüsen, H., Schumacher, S., Sieger, R., Tamlyn, J., Vogt, R., Vuilleumier, L., Xia, X., Ohmura, A., & König-Langlo, G. (2018). Baseline Surface Radiation Network (BSRN): structure and data description (1992–2017). *Earth System Science Data, 10*, 1491-1501

Duan, S.-B., Li, Z.-L., Cheng, J., & Leng, P. (2017a). Cross-satellite comparison of operational land surface temperature products derived from MODIS and ASTER data over bare soil surfaces. *Isprs Journal of Photogrammetry and Remote Sensing, 126*, 1-10

Duan, S.-B., Li, Z.-L., & Leng, P. (2017b). A framework for the retrieval of all-weather land surface temperature at a high spatial resolution from polar-orbiting thermal infrared and passive microwave data. *Remote Sensing of Environment, 195*, 107-117

Duan, S.-B., Li, Z.-L., Tang, B.-H., Wu, H., Tang, R., Bi, Y., & Zhou, G. (2014). Estimation of Diurnal Cycle of Land Surface Temperature at High Temporal and Spatial Resolution from Clear-Sky MODIS Data. *Remote Sensing, 6*, 3247-3262

Duan, S.-B., Li, Z.-L., Wang, N., Wu, H., & Tang, B.-H. (2012). Evaluation of six land-surface diurnal temperature cycle models using clear-sky in situ and satellite data. *Remote Sensing of Environment, 124*, 15-25

Duan, S.-B., Lian, Y., Zhao, E., Chen, H., Han, W., & Wu, Z. (2023). A Novel Approach to All-Weather LST Estimation Using XGBoost Model and Multisource Data. *IEEE Transactions on Geoscience and Remote Sensing, 61*, 1-14

Duan, S.B., Li, Z.L., Li, H., Gottsche, F.M., Wu, H., Zhao, W., Leng, P., Zhang, X., & Coll, C. (2019). Validation of Collection 6 MODIS land surface temperature product using in situ measurements. *Remote Sensing of Environment, 225*, 16-29

Ermida, S.L., DaCamara, C.C., Trigo, I.F., Pires, A.C., Ghent, D., & Remedios, J. (2017). Modelling directional effects on remotely sensed land surface temperature. *Remote Sensing of Environment, 190*, 56-69

Hersbach, H., Bell, B., Berrisford, P., Hirahara, S., Horányi, A., Muñoz-Sabater, J., Nicolas, J., Peubey, C., Radu, R., Schepers, D., Simmons, A., Soci, C., Abdalla, S., Abellan, X., Balsamo, G., Bechtold, P., Biavati, G., Bidlot, J., Bonavita, M., Chiara, G., Dahlgren, P., Dee, D., Diamantakis, M., Dragani, R., Flemming, J., Forbes, R., Fuentes, M., Geer, A., Haimberger, L., Healy, S., Hogan, R.J., Hólm, E., Janisková, M., Keeley, S., Laloyaux, P., Lopez, P., Lupu, C., Radnoti, G., Rosnay, P., Rozum, I., Vamborg, F.,

801 Villaume, S., & Thépaut, J.N. (2020). The ERA5 global reanalysis. *Quarterly Journal*
802 *of the Royal Meteorological Society, 146*, 1999-2049

803 Holmes, T.R.H., De Jeu, R.A.M., Owe, M., & Dolman, A.J. (2009). Land surface
804 temperature from Ka band (37 GHz) passive microwave observations. *Journal of*
805 *Geophysical Research, 114*

806 Hong, F., Zhan, W., Göttsche, F.-M., Lai, J., Liu, Z., Hu, L., Fu, P., Huang, F., Li,
807 J., Li, H., & Wu, H. (2021). A simple yet robust framework to estimate accurate daily
808 mean land surface temperature from thermal observations of tandem polar orbiters.
809 *Remote Sensing of Environment, 264*, 112612

810 Hong, F., Zhan, W., Göttsche, F.-M., Liu, Z., Dong, P., Fu, H., Huang, F., & Zhang,
811 X. (2022). A global dataset of spatiotemporally seamless daily mean land surface
812 temperatures: generation, validation, and analysis. *Earth System Science Data, 14*,
813 3091-3113

814 Inamdar, A.K., French, A., Hook, S., Vaughan, G., & Luckett, W. (2008). Land
815 surface temperature retrieval at high spatial and temporal resolutions over the
816 southwestern United States. *Journal of Geophysical Research, 113*

817 Jia, A., Liang, S., & Wang, D. (2022). Generating a 2-km, all-sky, hourly land
818 surface temperature product from Advanced Baseline Imager data. *Remote Sensing of*
819 *Environment, 278*, 113105

820 Jia, A., Liang, S., Wang, D., Ma, L., Wang, Z., & Xu, S. (2023). Global hourly,
821 5 km, all-sky land surface temperature data from 2011 to 2021 based on integrating
822 geostationary and polar-orbiting satellite data. *Earth System Science Data, 15*, 869-895

823 Jia, A., Ma, H., Liang, S., & Wang, D. (2021). Cloudy-sky land surface
824 temperature from VIIRS and MODIS satellite data using a surface energy balance-
825 based method. *Remote Sensing of Environment, 263*, 112566

826 Kalma, J.D., McVicar, T.R., & McCabe, M.F. (2008). Estimating land surface
827 evaporation: A review of methods using remotely sensed surface temperature data.
828 *Surveys in Geophysics, 29*, 421-469

829 Kappas, M., & Phan, T.N. (2018). Application of MODIS land surface temperature
830 data: a systematic literature review and analysis. *Journal of Applied Remote Sensing,*
831 *12*, 1

832 Kim, M., Brunner, D., & Kuhlmann, G. (2021). Importance of satellite
833 observations for high-resolution mapping of near-surface NO2 by machine learning.
834 *Remote Sensing of Environment, 264*, 112573

835 Lawrimore, J.H., Menne, M.J., Gleason, B.E., Williams, C.N., Wuertz, D.B., Vose,
836 R.S., & Rennie, J. (2011). An overview of the Global Historical Climatology Network
837 monthly mean temperature data set, version 3. *Journal of Geophysical Research, 116*

838 Li, B., Liang, S., Liu, X., Ma, H., Chen, Y., Liang, T., & He, T. (2021). Estimation
839 of all-sky 1 km land surface temperature over the conterminous United States. *Remote*
840 *Sensing of Environment, 266*, 112707

841 Li, B., Liang, S., Ma, H., Liu, X., He, T., & Zhang, Y. (2024). All-weather 1km
842 land surface temperature at global scale from 2000-2020 from MODIS data.Zenodo
843 [Data set]. Zenodo. https://doi.org/10.5281/zenodo.4292068

844 Li, J.-H., Li, Z.-L., Liu, X., & Duan, S.-B. (2023a). A global historical twice-daily

845 (daytime and nighttime) land surface temperature dataset produced by Advanced Very
846 High Resolution Radiometer observations from 1981 to 2021. *Earth System Science*
847 *Data, 15*, 2189-2212

848 Li, J.-H., Li, Z.-L., Liu, X., Duan, S.-B., Si, M., Shang, G., & Zhang, X. (2023b).
849 A generalized method for retrieving global daily mean land surface temperature from
850 polar-orbiting thermal infrared sensor instantaneous observations. *International*
851 *Journal of Remote Sensing*, 1-22

852 Li, X., Gong, P., Zhou, Y., Wang, J., Bai, Y., Chen, B., Hu, T., Xiao, Y., Xu, B.,
853 Yang, J., Liu, X., Cai, W., Huang, H., Wu, T., Wang, X., Lin, P., Li, X., Chen, J., He, C.,
854 Li, X., Yu, L., Clinton, N., & Zhu, Z. (2020). Mapping global urban boundaries from
855 the global artificial impervious area (GAIA) data. *Environmental Research Letters, 15*

856 Li, Z.-L., Tang, B.-H., Wu, H., Ren, H., Yan, G., Wan, Z., Trigo, I.F., & Sobrino,
857 J.A. (2013). Satellite-derived land surface temperature: Current status and perspectives.
858 *Remote Sensing of Environment, 131*, 14-37

859 Li, Z.L., Wu, H., Duan, S.B., Zhao, W., Ren, H., Liu, X., Leng, P., Tang, R., Ye,
860 X., Zhu, J., Sun, Y., Si, M., Liu, M., Li, J., Zhang, X., Shang, G., Tang, B.H., Yan, G.,
861 & Zhou, C. (2023c). Satellite Remote Sensing of Global Land Surface Temperature:
862 Definition, Methods, Products, and Applications. *Reviews of Geophysics, 61*

863 Liang, S., Cheng, J., Jia, K., Jiang, B., Liu, Q., Xiao, Z., Yao, Y., Yuan, W., Zhang,
864 X., Zhao, X., & Zhou, J. (2021). The Global Land Surface Satellite (GLASS) Product
865 Suite. *Bulletin of the American Meteorological Society, 102*, E323-E337

866 Liang, S., Zhang, X., Xiao, Z., Cheng, J., Liu, Q., & Zhao, X. (2013a). *Global*
867 *LAnd Surface Satellite (GLASS) products: algorithms, validation and analysis.*
868 Springer Science & Business Media

869 Liang, S., Zhao, X., Liu, S., Yuan, W., Cheng, X., Xiao, Z., Zhang, X., Liu, Q.,
870 Cheng, J., Tang, H., Qu, Y., Bo, Y., Qu, Y., Ren, H., Yu, K., & Townshend, J. (2013b).
871 A long-term Global LAnd Surface Satellite (GLASS) data-set for environmental studies.
872 *International Journal of Digital Earth, 6*, 5-33

873 Liu, Q., Wang, L., Qu, Y., Liu, N., Liu, S., Tang, H., & Liang, S. (2013a).
874 Preliminary evaluation of the long-term GLASS albedo product. *International Journal*
875 *of Digital Earth, 6*, 69-95

876 Liu, S., Li, X., Xu, Z., Che, T., Xiao, Q., Ma, M., Liu, Q., Jin, R., Guo, J., Wang,
877 L., Wang, W., Qi, Y., Li, H., Xu, T., Ran, Y., Hu, X., Shi, S., Zhu, Z., Tan, J., Zhang, Y.,
878 & Ren, Z. (2018). The Heihe Integrated Observatory Network: A Basin-Scale Land
879 Surface Processes Observatory in China. *Vadose Zone Journal, 17*, 180072

880 Liu, S.M., Xu, Z.W., Zhu, Z.L., Jia, Z.Z., & Zhu, M.J. (2013b). Measurements of
881 evapotranspiration from eddy-covariance systems and large aperture scintillometers in
882 the Hai River Basin, China. *Journal of Hydrology, 487*, 24-38

883 Liu, W., Cheng, J., & Wang, Q. (2023). Estimating Hourly All-Weather Land
884 Surface Temperature From FY-4A/AGRI Imagery Using the Surface Energy Balance
885 Theory. *IEEE Transactions on Geoscience and Remote Sensing, 61*, 1-18

886 Liu, X., Liang, S., Li, B., Ma, H., & He, T. (2021). Mapping 30 m Fractional Forest
887 Cover over China's Three-North Region from Landsat-8 Data Using Ensemble
888 Machine Learning Methods. *Remote Sensing, 13*, 2592

Liu, Y., Ackerman, S.A., Maddux, B.C., Key, J.R., & Frey, R.A. (2010). Errors in Cloud Detection over the Arctic Using a Satellite Imager and Implications for Observing Feedback Mechanisms. *Journal of Climate, 23*, 1894-1907

Long, D., Yan, L., Bai, L., Zhang, C., Li, X., Lei, H., Yang, H., Tian, F., Zeng, C., Meng, X., & Shi, C. (2020). Generation of MODIS-like land surface temperatures under all-weather conditions based on a data fusion approach. *Remote Sensing of Environment, 246*

Ma, J., Shen, H., Jiang, M., Lin, L., Meng, C., Zeng, C., Li, H., & Wu, P. (2024). A mechanism-guided machine learning method for mapping gapless land surface temperature. *Remote Sensing of Environment, 303*

Ma, J., Zhou, J., Göttsche, F.-M., Liang, S., Wang, S., & Li, M. (2020a). A global long-term (1981–2000) land surface temperature product for NOAA AVHRR. *Earth System Science Data, 12*, 3247-3268

Ma, L., Liu, Y., Zhang, X., Ye, Y., Yin, G., & Johnson, B.A. (2019). Deep learning in remote sensing applications: A meta-analysis and review. *Isprs Journal of Photogrammetry and Remote Sensing, 152*, 166-177

Ma, Y., Hu, Z., Xie, Z., Ma, W., Wang, B., Chen, X., Li, M., Zhong, L., Sun, F., Gu, L., Han, C., Zhang, L., Liu, X., Ding, Z., Sun, G., Wang, S., Wang, Y., & Wang, Z. (2020b). A long-term (2005–2016) dataset of hourly integrated land–atmosphere interaction observations on the Tibetan Plateau. *Earth Syst. Sci. Data, 12*, 2937-2957

Mao, K., Shi, J., Li, Z., Qin, Z., Li, M., & Xu, B. (2007). A physics-based statistical algorithm for retrieving land surface temperature from AMSR-E passive microwave data. *Science in China Series D: Earth Sciences, 50*, 1115-1120

Mao, K., Zuo, Z., Shen, X., Xu, T., Gao, C., & Liu, G. (2018). Retrieval of Land-surface Temperature from AMSR2 Data Using a Deep Dynamic Learning Neural Network. *Chinese Geographical Science, 28*, 1-11

McFarland, M.J., Miller, R.L., & Neale, C.M.U. (1990). Land surface temperature derived from the SSM/I passive microwave brightness temperatures. *IEEE Transactions on Geoscience and Remote Sensing, 28*, 839-845

Mercury, M., Green, R., Hook, S., Oaida, B., Wu, W., Gunderson, A., & Chodas, M. (2012). Global cloud cover for assessment of optical satellite observation opportunities: A HyspIRI case study. *Remote Sensing of Environment, 126*, 62-71

Metz, M., Rocchini, D., & Neteler, M. (2014). Surface Temperatures at the Continental Scale: Tracking Changes with Remote Sensing at Unprecedented Detail. *Remote Sensing, 6*, 3822-3840

Muñoz-Sabater, J., Dutra, E., Agustí-Panareda, A., Albergel, C., Arduini, G., Balsamo, G., Boussetta, S., Choulga, M., Harrigan, S., Hersbach, H., Martens, B., Miralles, D.G., Piles, M., Rodríguez-Fernández, N.J., Zsoter, E., Buontempo, C., & Thépaut, J.-N. (2021). ERA5-Land: a state-of-the-art global reanalysis dataset for land applications. *Earth System Science Data, 13*, 4349-4383

Ohmura, A., Gilgen, H., Hegner, H., Müller, G., Wild, M., Dutton, E.G., Forgan, B., Fröhlich, C., Philipona, R., Heimo, A., König-Langlo, G., McArthur, B., Pinker, R., Whitlock, C.H., & Dehne, K. (1998). Baseline Surface Radiation Network (BSRN/WCRP): New Precision Radiometry for Climate Research. *Bulletin of the*

American Meteorological Society, 79, 2115-2136

Østby, T.I., Schuler, T.V., & Westermann, S. (2014). Severe cloud contamination of MODIS Land Surface Temperatures over an Arctic ice cap, Svalbard. *Remote Sensing of Environment, 142*, 95-102

Pede, T., & Mountrakis, G. (2018). An empirical comparison of interpolation methods for MODIS 8-day land surface temperature composites across the conterminous Unites States. *Isprs Journal of Photogrammetry and Remote Sensing, 142*, 137-150

Qu, Y., Liang, S., Liu, Q., Li, X., Feng, Y., & Liu, S. (2016). Estimating Arctic sea-ice shortwave albedo from MODIS data. *Remote Sensing of Environment, 186*, 32-46

Qu, Y., Liu, Q., Liang, S., Wang, L., Liu, N., & Liu, S. (2014). Direct-Estimation Algorithm for Mapping Daily Land-Surface Broadband Albedo From MODIS Data. *IEEE Transactions on Geoscience and Remote Sensing, 52*, 907-919

Rao, Y., Liang, S., Wang, D., Yu, Y., Song, Z., Zhou, Y., Shen, M., & Xu, B. (2019). Estimating daily average surface air temperature using satellite land surface temperature and top-of-atmosphere radiation products over the Tibetan Plateau. *Remote Sensing of Environment, 234*, 111462

Shen, H., Jiang, Y., Li, T., Cheng, Q., Zeng, C., & Zhang, L. (2020). Deep learning-based air temperature mapping by fusing remote sensing, station, simulation and socioeconomic data. *Remote Sensing of Environment, 240*

Shiff, S., Helman, D., & Lensky, I.M. (2021). Worldwide continuous gap-filled MODIS land surface temperature dataset. *Sci Data, 8*, 74

Stokes, G.M., & Schwartz, S.E. (1994). The Atmospheric Radiation Measurement (ARM) Program: Programmatic Background and Design of the Cloud and Radiation Test Bed. *Bulletin of the American Meteorological Society, 75*, 1201-1221

Sun, D., & Pinker, R.T. (2005). Implementation of GOES-based land surface temperature diurnal cycle to AVHRR. *International Journal of Remote Sensing, 26*, 3975-3984

Tang, W., Zhou, J., Ma, J., Wang, Z., Ding, L., Zhang, X., & Zhang, X. (2024). TRIMS LST: a daily 1 km all-weather land surface temperature dataset for China's landmass and surrounding areas (2000–2022). *Earth System Science Data, 16*, 387-419

Tomlinson, C.J., Chapman, L., Thornes, J.E., & Baker, C. (2011). Remote sensing land surface temperature for meteorology and climatology: a review. *Meteorological Applications, 18*, 296-306

Townshend, J.R.G., Justice, C.O., Skole, D., Malingreau, J.P., Cihlar, J., Teillet, P., Sadowski, F., & Ruttenberg, S. (2007). The 1 km resolution global data set: needs of the International Geosphere Biosphere Programme†. *International Journal of Remote Sensing, 15*, 3417-3441

Wan, Z. (2014). New refinements and validation of the collection-6 MODIS land-surface temperature/emissivity product. *Remote Sensing of Environment, 140*, 36-45

Wan, Z., & Li, Z.-L. (1997). A physics-based algorithm for retrieving land-surface emissivity and temperature from EOS/MODIS data. *IEEE Transactions on Geoscience and Remote Sensing, 35*, 980-996

Wan, Z., Wang, P., & Li, X. (2010). Using MODIS Land Surface Temperature and

Normalized Difference Vegetation Index products for monitoring drought in the southern Great Plains, USA. *International Journal of Remote Sensing, 25*, 61-72

Wang, N., Tang, B.-H., Li, C., & Li, Z.-L. (2010). A generalized neural network for simultaneous retrieval of atmospheric profiles and surface temperature from hyperspectral thermal infrared data, 1055-1058

Weng, Q. (2009). Thermal infrared remote sensing for urban climate and environmental studies: Methods, applications, and trends. *Isprs Journal of Photogrammetry and Remote Sensing, 64*, 335-344

Williamson, S., Hik, D., Gamon, J., Kavanaugh, J., & Flowers, G. (2014). Estimating Temperature Fields from MODIS Land Surface Temperature and Air Temperature Observations in a Sub-Arctic Alpine Environment. *Remote Sensing, 6*, 946-963

Wu, P., Su, Y., Duan, S.-b., Li, X., Yang, H., Zeng, C., Ma, X., Wu, Y., & Shen, H. (2022). A two-step deep learning framework for mapping gapless all-weather land surface temperature using thermal infrared and passive microwave data. *Remote Sensing of Environment, 277*

Wu, P., Yin, Z., Zeng, C., Duan, S., Gottsche, F.-M., Ma, X., Li, X., Yang, H., & Shen, H. (2019). Spatially Continuous and High-resolution Land Surface Temperature: A Review of Reconstruction and Spatiotemporal Fusion Techniques. *arXiv preprint arXiv:1909.09316*

Xing, Z., Li, Z.-L., Duan, S.-B., Liu, X., Zheng, X., Leng, P., Gao, M., Zhang, X., & Shang, G. (2021). Estimation of daily mean land surface temperature at global scale using pairs of daytime and nighttime MODIS instantaneous observations. *Isprs Journal of Photogrammetry and Remote Sensing, 178*, 51-67

Xu, S., & Cheng, J. (2021). A new land surface temperature fusion strategy based on cumulative distribution function matching and multiresolution Kalman filtering. *Remote Sensing of Environment, 254*, 112256

Yamamoto, S. (2005). Findings through the AsiaFlux network and a view toward the future. *Journal of Geographical Sciences, 15*, 142

Yao, R., Wang, L., Huang, X., Cao, Q., Wei, J., He, P., Wang, S., & Wang, L. (2023). Global seamless and high-resolution temperature dataset (GSHTD), 2001–2020. *Remote Sensing of Environment, 286*

Yao, Y., Liang, S., Qin, Q., Wang, K., Liu, S., & Zhao, S. (2012). Satellite detection of increases in global land surface evapotranspiration during 1984-2007. *International Journal of Digital Earth, 5*, 299-318

Yu, P., Zhao, T., Shi, J., Ran, Y., Jia, L., Ji, D., & Xue, H. (2022). Global spatiotemporally continuous MODIS land surface temperature dataset. *Sci Data, 9*, 143

Yu, W., Ma, M., Wang, X., & Tan, J. (2014). Estimating the land-surface temperature of pixels covered by clouds in MODIS products. *Journal of Applied Remote Sensing, 8*, 083525

Yuan, Q., Shen, H., Li, T., Li, Z., Li, S., Jiang, Y., Xu, H., Tan, W., Yang, Q., Wang, J., Gao, J., & Zhang, L. (2020). Deep learning in environmental remote sensing: Achievements and challenges. *Remote Sensing of Environment, 241*

Zeng, C., Long, D., Shen, H., Wu, P., Cui, Y., & Hong, Y. (2018). A two-step

framework for reconstructing remotely sensed land surface temperatures contaminated by cloud. *Isprs Journal of Photogrammetry and Remote Sensing, 141*, 30-45

Zhang, D., Tang, R., Tang, B.-H., Wu, H., & Li, Z.-L. (2015). A Simple Method for Soil Moisture Determination From LST–VI Feature Space Using Nonlinear Interpolation Based on Thermal Infrared Remotely Sensed Data. *IEEE Journal of Selected Topics in Applied Earth Observations and Remote Sensing, 8*, 638-648

Zhang, H., Tang, B.-H., & Li, Z.-L. (2024). A practical two-step framework for all-sky land surface temperature estimation. *Remote Sensing of Environment, 303*

Zhang, Q., Yuan, Q., Zeng, C., Li, X., & Wei, Y. (2018). Missing Data Reconstruction in Remote Sensing Image With a Unified Spatial–Temporal–Spectral Deep Convolutional Neural Network. *IEEE Transactions on Geoscience and Remote Sensing, 56*, 4274-4288

Zhang, T., Zhou, Y., Zhu, Z., Li, X., & Asrar, G.R. (2022). A global seamless 1 km resolution daily land surface temperature dataset (2003–2020). *Earth System Science Data, 14*, 651-664

Zhang, X., Wang, D., Liu, Q., Yao, Y., Jia, K., He, T., Jiang, B., Wei, Y., Ma, H., & Zhao, X. (2019). An operational approach for generating the global land surface downward shortwave radiation product from MODIS data. *IEEE Transactions on Geoscience and Remote Sensing, 57*, 4636-4650

Zhang, X., Zhou, J., Liang, S., Chai, L., Wang, D., & Liu, J. (2020). Estimation of 1-km all-weather remotely sensed land surface temperature based on reconstructed spatial-seamless satellite passive microwave brightness temperature and thermal infrared data. *Isprs Journal of Photogrammetry and Remote Sensing, 167*, 321-344

Zhang, X., Zhou, J., Liang, S., & Wang, D. (2021). A practical reanalysis data and thermal infrared remote sensing data merging (RTM) method for reconstruction of a 1-km all-weather land surface temperature. *Remote Sensing of Environment, 260*, 112437

Zhang, Y., Liang, S., Ma, H., He, T., Wang, Q., Li, B., Xu, J., Zhang, G., Liu, X., & Xiong, C. (2023). Generation of global 1 km daily soil moisture product from 2000 to 2020 using ensemble learning. *Earth System Science Data, 15*, 2055-2079

Zhao, W., Duan, S.-B., Li, A., & Yin, G. (2019). A practical method for reducing terrain effect on land surface temperature using random forest regression. *Remote Sensing of Environment, 221*, 635-649

Zhou, D., Xiao, J., Bonafoni, S., Berger, C., Deilami, K., Zhou, Y., Frolking, S., Yao, R., Qiao, Z., & Sobrino, J. (2018). Satellite Remote Sensing of Surface Urban Heat Islands: Progress, Challenges, and Perspectives. *Remote Sensing, 11*, 48

Zhou, J., Dai, F., Zhang, X., Zhao, S., & Li, M. (2015). Developing a temporally land cover-based look-up table (TL-LUT) method for estimating land surface temperature based on AMSR-E data over the Chinese landmass. *International Journal of Applied Earth Observation and Geoinformation, 34*, 35-50

Zhou, S., Cheng, J., & Shi, J. (2022). A Physical-Based Framework for Estimating the Hourly All-Weather Land Surface Temperature by Synchronizing Geostationary Satellite Observations and Land Surface Model Simulations. *IEEE Transactions on Geoscience and Remote Sensing, 60*, 1-22

1065